

Detection and Identification of Effluent Gases Using Invariant Hyperspectral Algorithms

by

Erin O'Donnell

B.S. Rochester Institute of Technology (2001)

A thesis submitted in partial fulfillment of the
requirements for the degree of Master of Science
in the Chester F. Carlson Center for Imaging Science
Rochester Institute of Technology

August 2005

Signature of the Author _____

Accepted by _____
Coordinator, M.S. Degree Program Date

CHESTER F. CARLSON CENTER FOR IMAGING SCIENCE
ROCHESTER INSTITUTE OF TECHNOLOGY
ROCHESTER, NEW YORK

CERTIFICATE OF APPROVAL

M.S. DEGREE THESIS

The M.S. Degree Thesis of Erin O'Donnell
has been examined and approved by the
thesis committee as satisfactory for the
thesis required for the
M.S. degree in Imaging Science

Carl Salvaggio, Ph.D., Thesis Advisor

David Messinger, Ph.D.

John Schott, Ph.D.

Date

THESIS RELEASE PERMISSION
ROCHESTER INSTITUTE OF TECHNOLOGY
CHESTER F. CARLSON CENTER FOR IMAGING SCIENCE

Title of Thesis:

**Detection and Identification of Effluent Gases Using Invariant
Hyperspectral Algorithms**

I, Erin O'Donnell, hereby grant permission to Wallace Memorial Library of R.I.T. to reproduce my thesis in whole or in part. Any reproduction will not be for commercial use or profit.

Signature _____ Date _____

Detection and Identification of Effluent Gases Using Invariant Hyperspectral Algorithms

by

Erin O'Donnell

Submitted to the
Chester F. Carlson Center for Imaging Science
in partial fulfillment of the requirements
for the Master of Science Degree
at the Rochester Institute of Technology

Abstract

The ability to detect and identify effluent gases is a problem that has been pursued with limited success. An algorithm to do this would not only aid in the regulation of pollutants but also in treaty enforcement. Considering these applications, finding a way to remotely investigate a gaseous emission is highly desirable. This research utilizes hyperspectral imagery in the infrared region of the electromagnetic spectrum to evaluate invariant methods of detecting and identifying gases within a scene. The image is evaluated on a pixel-by-pixel basis and is also studied at the subpixel level. A library of target gas spectra is generated using a simple radiance model. This results in a more robust representation of the gas spectra which are representative of real-world observations. This library is the subspace utilized by the detection and identification algorithm. An evaluation was carried out to determine the subset of basis vectors that best span the subspace. Two basis vector selection methods are used to determine the subset of basis vectors; Singular Value Decomposition (SVD) and the Maximum Distance Method (MaxD). The Generalized Likelihood Ratio Test (GLRT) was used to determine whether the pixel is more like the target or the background. The target can be either a single species or a combination of gases, however, this study only looks for

one gas at a time. Synthetically generated hyperspectral scenes in the longwave infrared (LWIR) region of the electromagnetic spectrum are used for this research. The test scenarios used in this study represented strong and weak plumes with single or multiple gas releases. In this work, strong and weak plumes refer to the release, which is on the order of tens of grams per second and tenths of grams per second, respectively. This work demonstrates the effectiveness of these invariant algorithms for the gas detection and identification problem.

Acknowledgements

I would not have been able to accomplish this work without the love and support of my family, especially; my parents, Susan and Joseph Smith, and my grandfather, Thomas Linnan.

I was lucky to have had the privilege to work with the best committee. They have been the most supportive people of my research and career; without the combined efforts of these advisors this work would not be what it is. Specifically thanks to:

Dr. John Schott for taking me under your wing and guiding me from the onset when I was just a confused undergraduate. I am grateful for all the knowledge and opportunities you have given me.

Dr. David Messinger for always being there for me; you were the best “go” to guy whether you wanted to be or not. Thanks for being able to cut through my nonsense, keep me focused, and teach me a tremendous amount in the meantime. There is something to be said about getting “stuck” with the new guy.

Dr. Carl Salvaggio for always having my best interest in mind even when it meant more work for me. I am ultimately grateful you had me do it. I only wish I had the opportunity to take classes with you. I am very appreciative to have had the opportunity to work with you and have you as my advisor.

Contents

List of Figures	xiii
1 Introduction	1
1.1 Objective	1
1.2 Invariant Methodology	5
2 Background and Literature Review	6
2.1 SVD Detection	6
2.1.1 Singular Value Decomposition	7
2.2 Detection and Quantification	8
2.3 Invariant Algorithms	12
2.4 Algorithm Applicability	16
3 Approach	18
3.1 Radiance Model	18
3.1.1 Beer's Law	20
3.2 Description of the Invariant Target Space	21
3.3 Test Data	25
3.3.1 Plume Emission and Absorption Implementation	26
3.4 Basis Vectors	27

4	Results	34
4.1	Analysis	34
4.2	Library Size	37
4.3	SVD vs. MaxD	44
4.4	Case 4	46
4.4.1	Atmospheric Mismatch	51
4.5	Case 7	55
4.6	Case 5	56
4.7	Case 6	59
5	Conclusion	70
6	Future Work	73

List of Figures

1.1	On the left side of the SF_6 feature the spectrum at 5°C has the highest magnitude and on the right the spectrum at 50°C has the highest magnitude.	3
1.2	This graph of NH_3 target spectra shows the differences in the absorption spectrum when the concentration varies from 1-1000 ppm-m.	4
2.1	These photon paths were neglected by Young; a) reflected atmospheric downwelled off the surface, b) reflected atmospheric downwelled off the plume, c) plume downwelled off the surface	10
2.2	a) The vectors are showing the points furthest from the origin and closest to the origin. b) The dotted vector represents the difference vector. c) A plane is found perpendicular to the difference vector. d) The data can then be projected onto the new plane. e) This n -dimensional representation of the data shows the basis vectors at the corners of the simplex	15
3.1	The self-emitted energy paths are: f) self-emitted, g) background self-emitted, h) self-emitted reflected by background, i) downwelled, j) upwelled.	19

3.2	This represents the radiance model that will be used to describe this problem.	22
3.3	Atmospheric transmission used in this study	23
3.4	Atmospheric radiance used in this study	23
3.5	This represents the column effects, where the different layers represent the varying parameters of the plume.	24
3.6	Simplification of the Gaussian plume model (smooth curve); for the single slab (single rect) and multi-slab (multiple rects) cases.	25
3.7	A band at $10.73 \mu\text{m}$ from the test scene that was used.	27
3.8	Spatially Enhanced Broadband Array Spectrograph System (SEBASS) noise covariance image.	28
3.9	The temperature of the plume can be represented by the surface temperature plus some offset.	28
3.10	The extremes of the Freon-114 target spectral library. The top spectrum shows the target gas in emission, while the bottom is in absorption. . .	29
3.11	The top 10 target basis vectors, which were used in this study, for Freon-114 as defined by singular value decomposition (SVD) and determined from a target library of nine temperatures and eight concentrations. (Note: The structure in the first basis vector is not seen; it was compressed due to the other offset plots.)	30
3.12	The top 10 target basis vectors, which were used in this study, for Freon-114 as defined by maximum distance method (MaxD) and determined from a target library of nine temperatures and eight concentrations. . .	31
3.13	The top 15 background basis vectors, which were used in this study, for the background as defined by SVD. (Note: The structure in the first basis vector is not seen; it was compressed due to the other offset plots.)	32

3.14	The top 15 background basis vectors, which were used in this study, for the background as defined by MaxD.	33
4.1	Case 4, Freon-114 band results using SVD for each of the libraries, where the indices correspond to the libraries as listed in Table 4.2. The points represent the standard deviation.	38
4.2	Case 4, Freon-114 band results using MaxD for each of the libraries, where the points represent the standard deviation.	39
4.3	Case 4, ammonia band results using SVD for each of the libraries, where the points represent the standard deviation.	40
4.4	Case 4, ammonia band results using MaxD for each of the libraries, where the points represent the standard deviation.	41
4.5	Case 5, ammonia band results using SVD for each of the libraries, where the points represent the standard deviation.	42
4.6	Case 5, ammonia band results using MaxD for each of the libraries, where the points represent the standard deviation.	43
4.7	Normalized GLRT results for the Freon-114 band, which used SVD for basis vector selection.	45
4.8	Normalized GLRT results for the Freon-114 band, which used MaxD for basis vector selection.	46
4.9	Detection profile for the Freon-114 plume region, which used SVD for basis vector selection.	47
4.10	Detection profile for the Freon-114 plume region, which used MaxD for basis vector selection.	47
4.11	Normalized GLRT results for the ammonia band of Case 2, which used SVD for basis vector selection.	48
4.12	Normalized GLRT results for the ammonia band of Case 2, which used MaxD for basis vector selection.	49

4.13	Detection profile for the ammonia plume region of Case 2, which used SVD for basis vector selection.	50
4.14	Detection profile for the ammonia plume region of Case 2, which used MaxD for basis vector selection.	50
4.15	Normalized GLRT results for the Freon-114 band of Case 4, a weak release.	51
4.16	Detection profile for the Freon-114 plume region of Case 4, a weak release.	52
4.17	Detection profile for the ammonia plume region of Case 4, a weak release.	52
4.18	Normalized GLRT results for the ammonia band of Case 4, a weak release.	53
4.19	Normalized GLRT results for the SF ₆ band of Case 4, a weak release. .	53
4.20	Detection profile for the Freon-114 plume region of Case 4, a weak release, using target spectra with an atmosphere that does not match that of the scene.	55
4.21	Detection profile for the ammonia plume region of Case 4, a weak release, using target spectra with an atmosphere that does not match that of the scene.	56
4.22	Normalized GLRT results for the Freon-114 band of Case 4, a weak release, using target spectra with an atmosphere that does not match that of the scene.	57
4.23	Normalized GLRT results for the ammonia band of Case 4, a weak re- lease, using target spectra with an atmosphere that does not match that of the scene.	58
4.24	Detection profile for the ammonia plume region of Case 4, a weak release, using target spectra which do not incorporate atmospheric parameters. .	59
4.25	Detection profile for the ammonia plume region of Case 4, a weak release, using target spectra which do not incorporate atmospheric parameters. .	60
4.26	Detection profile for fluorobenzene the plume region of Case 7, a weak release.	61

4.27	Normalized GLRT results for the fluorobenzene band of Case 7, a weak release.	62
4.28	Detection profile for the phosgene plume region of Case 7, a weak release.	62
4.29	Normalized GLRT results for the phosgene band of Case 7, a weak release.	63
4.30	Detection profile for the plume region of Case 5, a weak release.	63
4.31	Normalized GLRT results for the ammonia band of Case 5, a weak release.	64
4.32	Normalized GLRT results for the 1,1,2,2-tetrachloroethane band of Case 5, a weak release.	65
4.33	Raw absorption spectrum of 1,1,2,2-tetrachloroethane	66
4.34	Target spectrum for 1,1,2,2-tetrachloroethane at 51°C and 1000 ppm-m	66
4.35	Detection profile for the 1,2-dichloropropane plume region of Case 6, a weak release.	67
4.36	Normalized GLRT results for the 1,2-dichloropropane band of Case 6, a weak release.	68
4.37	Detection profile for the methane plume region of Case 6, a weak release.	68
4.38	Normalized GLRT results for the methane band of Case 6, a weak release.	69
4.39	Raw absorption spectrum for methane.	69
5.1	Raw absorption spectra for ammonia and sulfur hexafluoride.	71
5.2	Target spectra for ammonia and sulfur hexafluoride.	71

Acronyms

Throughout this paper there will be a number of acronyms used. The following list can be a quick reference to deciphering these acronyms.

ARES Airborne Remote Earth Sensing. The program which ran the testing at the Navajo Generating Station.

CIS Center for Imaging Science

DIRSIG Digital Imaging and Remote sensing Synthetic Image Generator. The Digital Imaging and Remote sensing Synthetic Image Generator (DIRSIG) ray tracing environment was developed by Center for Imaging Science (CIS) at Rochester Institute of Technology (RIT).

EPA Environmental Protection Agency

GLRT generalized likelihood ratio test

ISAC In-Scene Atmospheric Compensation

JPL Jet Propulsion Laboratory

LWIR longwave infrared

MaxD maximum distance method

MODTRAN Moderate Resolution Transmittance: atmospheric model

MWIR midwave infrared

RIT Rochester Institute of Technology

ROI region of interest

SEBASS Spatially Enhanced Broadband Array Spectrograph System

SVD singular value decomposition

SWIR shortwave infrared

Chapter 1

Introduction

Effluent gases are the end product of many chemical processes. These processes could be simple combustion used to heat a building or generate power, or a more complex process reminiscent of chemical production. The Environmental Protection Agency (EPA) regulates air emissions, but monitoring this can be difficult. Taking an air sample would be ideal; however, this is not always possible. Various state and local agencies would like to know what a facility is making just by looking at the emissions from a stack or vent. It would be useful to be able to assist these types of organizations with an algorithm that would extract the desired information from imagery.

Algorithm utility for the effluent gas problem involves detecting and locating the gas cloud, identifying the gas species, quantifying the mixing ratio, and ultimately, concentration prediction. The focus of this research was on the detection and identification components of the algorithm development process.

1.1 Objective

The intention for this work was to evaluate an algorithm for this gas detection and identification problem using hyperspectral image data. The algorithm of interest, the

Invariant Algorithm, was developed to be unaffected by changes in atmospheric and illumination conditions[5],[16]. This work utilizes the invariant nature of this algorithm to neglect temperature and concentration variations within a gas cloud. The algorithm utilized is implemented in two ways. The first utilizes singular value decomposition (SVD) to select basis vectors and the second utilizes the maximum distance method (MaxD)[8] to select basis vectors.

Basis vectors are determined from a data set, which in this case is derived from imagery or target gases. The basis vectors “span” the space the data set represents. These algorithms reorganize the data such that the resulting basis vectors are statistically independent and ordered such that the important information is brought to the front. This allows for a reduced set to be taken, which still encapsulates most of the variability in the data and reduces processing time. A weighted linear combination of basis vectors can recreate the original data set. Since the number of basis vectors are being reduced some error will be introduced when recreating the original data space.

The Healey-Invariant Algorithm[5] has two implementations for basis vector selection; the fully-resolved and the sub-pixel implementation. The fully-resolved implementation looks for the target while the sub-pixel implementation looks for target within the background. The Lee Algorithm[8] is intrinsically a sub-pixel algorithm. Plumes are inherently transmissive, so, the sub-pixel version of the Healey and the Lee Algorithm were used to see which would provide a better solution for the gas detection and identification problem.

The problem that is faced in gas detection and identification is that the spectrum of the gas to be detected will look different with varying temperatures, concentrations, and backgrounds. Figure 1.1 illustrates that when the temperature of a gas increases, the spectral features do not simply scale in magnitude, the overall shape of the feature may change. This complexity is also seen in Figure 1.2 when the concentrations are

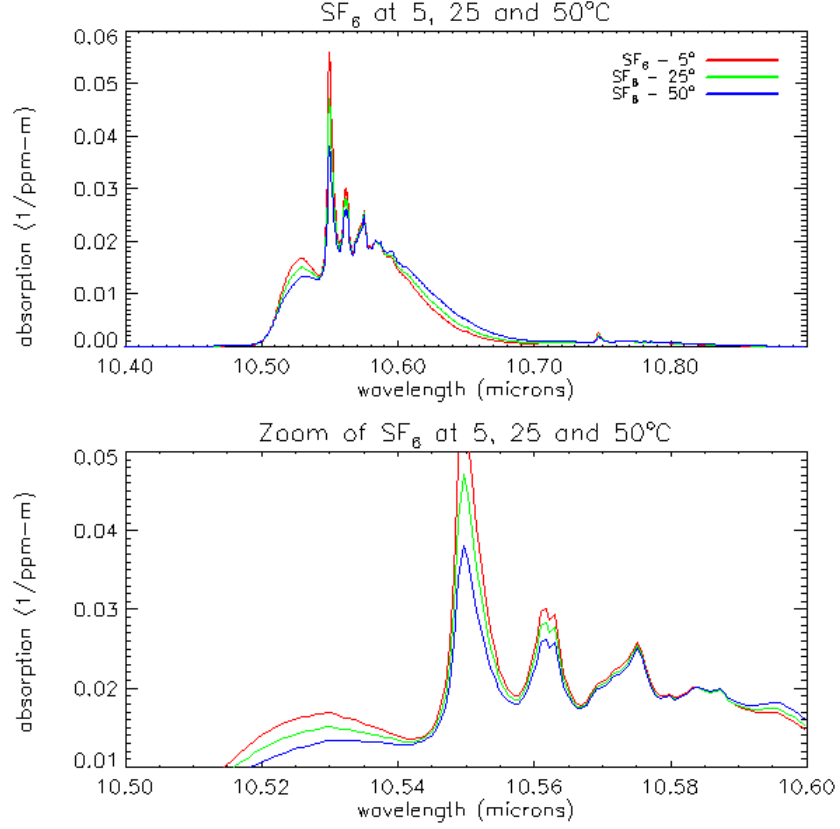
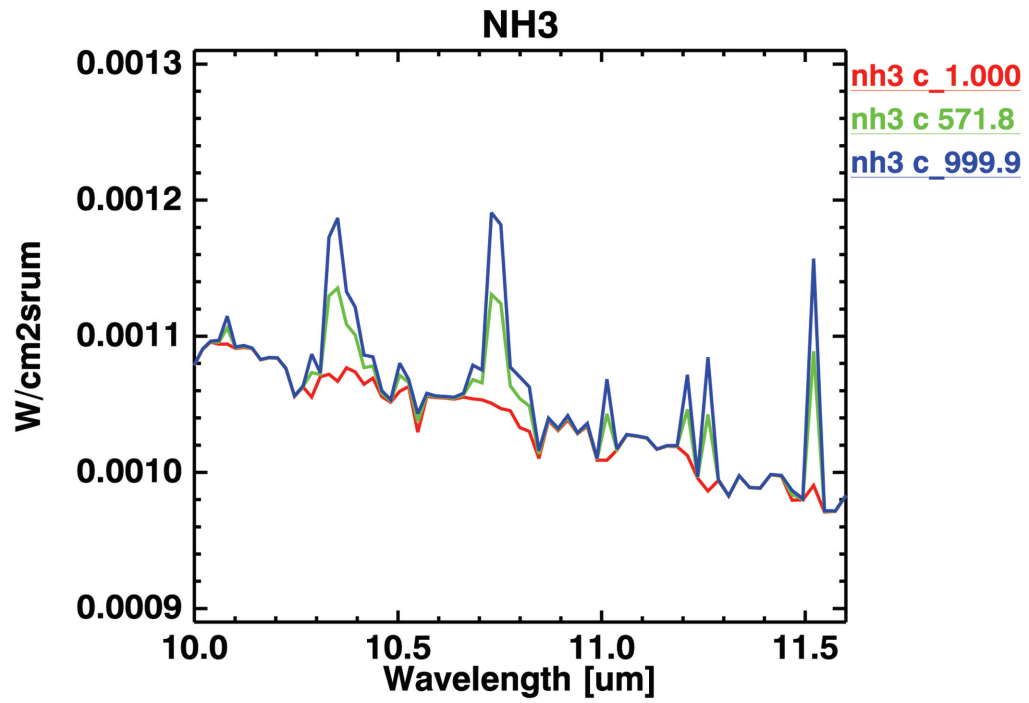


Figure 1.1: On the left side of the SF_6 feature the spectrum at 5°C has the highest magnitude and on the right the spectrum at 50°C has the highest magnitude.

varied. These features are further altered when they are sensed over a terrestrial background, whose temperature and spectrum will affect the appearance of the resultant gas spectrum.

The remainder of this document will discuss; first, the methodology of the Invariant Algorithm, second, previous work done on this problem and in what way that work supported this research, third, the process followed in this work along with the supporting theory, and finally the results and conclusions will be presented.



..

Figure 1.2: This graph of NH₃ target spectra shows the differences in the absorption spectrum when the concentration varies from 1-1000 ppm-m.

1.2 Invariant Methodology

Target detection is usually accomplished by converting a scene into an alternative vector space where the individual pixel radiance vectors look most like the targets of interest. For example, in the reflective spectral region the atmosphere is often compensated for and the radiance data converted to reflectance because this new space most closely resembles the conditions where the target spectrum was observed. This would allow for target detection since the vector more closely resembles the known target spectrum. However, in gas detection, the target is transparent and compensation for the atmosphere results in a chance that the target signature will be altered. The traditional method, as a result, may not be optimal for gases because the target gases can be transparent and influenced by its surroundings. Most notably the target can be seen in absorption or emission where the gas is either absorbing energy from the surround or releasing energy to the surround. Both the Lee and the Healey invariant methods model the target in the various ways that it would be seen in the sensed image space. For example in this study, the atmosphere is added to the target and the gas concentrations and temperatures are varied creating a library of possible radiance vectors. All target variations in a dataset can be represented by defining a reduced set of basis vectors, linear combinations of which will recreate the original dataset. The reduced set of vectors are used solely for limiting time consumption. A dataset can be reduced by several means; SVD, MaxD, principal components, etc. Target basis vectors are generated from the library of modeled target spectra. Background basis vectors are generated from a region of the test image where no targets are assumed to be present. The test scene is evaluated using the Generalized Likelihood Ratio Test (GLRT) that will determine whether each pixel is more like the background or the target gas. A test pixel is evaluated using the basis vectors and the GLRT.

Chapter 2

Background and Literature Review

2.1 SVD Detection

In 1996, Lisowski and Cook [9] assessed the use of shortwave infrared (SWIR) and mid-wave infrared (MWIR) hyperspectral imagery collected under the Airborne Remote Earth Sensing (ARES) program, to identify SO_2 being emitted from a coal burning power plant. Their study evaluated three algorithms for determining the presence of this chemical: SVD, linearly-normalized band differencing, and Planckian-normalized band differencing. Linearly-normalized and Planckian-normalized band differencing is carried out by subtracting the spectrum of a background and plume pixel spectrum yielding a residual spectrum. The linearly-normalized method removes a background pixel that does not contain the gas while Planckian-normalization subtracts a Planck curve that has been fit to the data. Both of these methods result in a spectrum that would allow the features of the gas, if present, to be more evident. The results of this study showed that SVD can be used to determine the extent or area of the chemical plume from ground collected imagery. The differencing techniques were useful for identi-

fication of SO_2 . The Planckian-normalization technique provided an enhanced contrast in the emission feature over the linearly-normalized method because the background pixel used in the linear-normalized technique had to be selected in close proximity to the stack. However, the background pixel selected may not have been the same as the background under the plume and since it was a background pixel close to the stack it may have been a mixed pixel with the gas, resulting in a less distinct spectrum.

2.1.1 Singular Value Decomposition

“Given a set of observations, one often wants to condense and summarize the data by fitting it to a ‘model’ that depends on adjustable parameters.”[13] Singular value decomposition does just that by means of eigenvector decomposition.

The data is rotated into a space where most of the important information is brought to the front. To understand the mathematics of SVD some background is necessary. Consider square matrix \mathbf{A}_{sq} , that can be rewritten, or spectrally decomposed as,

$$\mathbf{A}_{sq} = \mathbf{U}\mathbf{\Lambda}\mathbf{U}^T, \quad (2.1)$$

where \mathbf{U} has the property,

$$\mathbf{U}^T\mathbf{\Lambda}\mathbf{U} = \mathbf{I}; \quad (2.2)$$

\mathbf{I} is the identity matrix and $\mathbf{\Lambda}$ is the diagonalized eigenvalue matrix. For a non-square matrix, \mathbf{A} , another means of decomposing is necessary, hence SVD is used.

The equation for SVD is as follows:

$$\mathbf{A} = \mathbf{U}\mathbf{W}(\mathbf{V}^T), \quad (2.3)$$

where \mathbf{A} is the original image matrix with physical dimensions M pixels x N bands, \mathbf{U} is as described previously in Equation 2.2 and \mathbf{V} is also,

$$\mathbf{V}^T \mathbf{V} = \mathbf{I}. \quad (2.4)$$

Matrices \mathbf{U} and \mathbf{V} are orthogonal with dimensions $M \times N$ and $N \times N$ respectively. Matrix \mathbf{W} , similar to $\mathbf{\Lambda}$, is a diagonal matrix comprised of N singular values, w_i ($i=1,2,\dots,N$), which are the square root of eigenvalues, as seen in Equation 2.5.

$$\mathbf{W} = \begin{pmatrix} w_1 & 0 & \cdots & 0 \\ 0 & w_2 & & \\ \vdots & & \ddots & \\ 0 & & & w_N \end{pmatrix} \quad (2.5)$$

Here \mathbf{U} contains the uncorrelated basis vectors from which a subset can be selected in order to work with a reduced dataset. This new reduced data set, while smaller, contains most of the important information from the original.[13][10][15]

2.2 Detection and Quantification

In 2002, Young [17] reviewed processes for gas detection and quantification. That research utilized SEBASS data collected over a commercial refinery's stacks to study point source emissions of carbon dioxide. The SEBASS instrument is a hyperspectral spectrometer that images in the MWIR (3–5 μm) and longwave infrared (LWIR) (7.5–13.6 μm) regions of the electromagnetic spectrum. It has a resolution of about 0.025 μm in the MWIR and about 0.05 μm in the LWIR. Young's study utilized the LWIR spectrometer data. The last four channels were not operable, restricting the spectral

coverage to wavelengths shorter than $13.42 \mu\text{m}$. The resultant images were radiometrically calibrated.

Young's study expected to find ammonia, carbon dioxide, ethylene, methane, nitrogen dioxide, nitrous oxide, sulfur dioxide, and water vapor. They were all determined to be present. The radiance expression used for the target data was a linear model expressed in terms of the background spectra and the gas absorption spectra. The background spectra were determined from three methods, in-scene spectra, image cluster spectra and eigenvectors from spectral clutter covariances. The gas absorption spectra were taken from a commercially available library of laboratory spectra measured at a reference temperature of 20°C .

In Young's implementation of the radiance model, atmospheric downwelling radiance reflected off of the surface and the plume were neglected as well as downwelling plume radiance off the surface, as shown in Figure 2.1. The background was approximated as a blackbody, with a high emissivity. The plumes are modeled as optically thin, and therefore can utilize Beer's Law; which defines the transmission of the plume. The reason for this will be discussed in a later section. Young's model does not, however, leave room for native gases (atmospheric gases). It does attempt to compensate for them but the article states the model is not sufficient for strong atmospheric absorbers. Atmospheric compensation was done on the SEBASS data using the In-Scene Atmospheric Compensation (ISAC) algorithm[17].

The detection analysis done on the imagery used principal components. The principal components algorithm results in orthogonal component images that sort the information from highest to lowest radiance variability. The principal components algorithm, driven by image covariance, was able to find significant plumes in imagery that had yet to be atmospherically corrected. Significant plumes are those which have a high temperature contrast or a wide spatial distribution that would provide enough signal

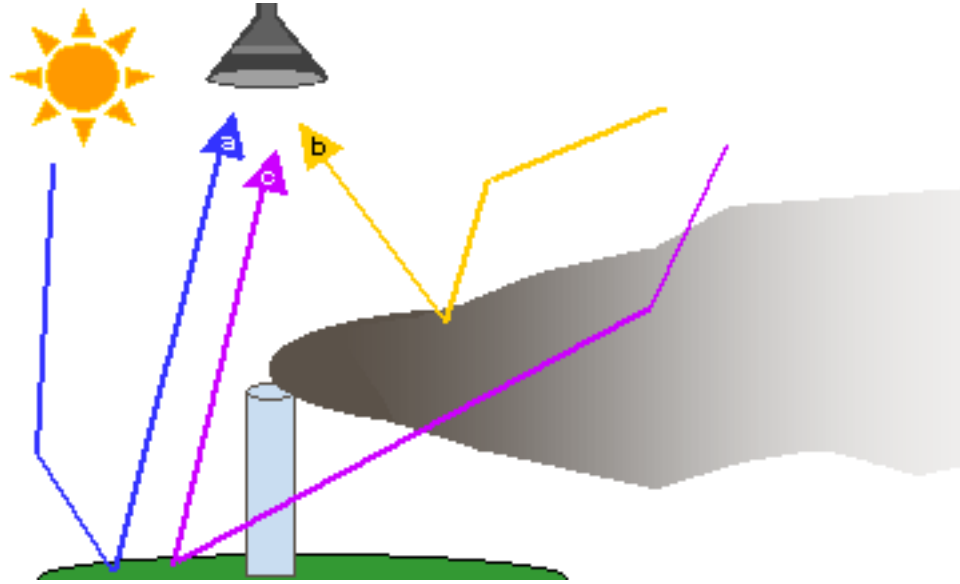


Figure 2.1: These photon paths were neglected by Young; a) reflected atmospheric downwelled off the surface, b) reflected atmospheric downwelled off the plume, c) plume downwelled off the surface

variation to be spotted in the component images. The article does not specify which is the case. While the algorithm did find plumes, they were not the only things that were returned in the component image. It was still necessary for a supervised inspection to determine what was a plume and what was background clutter. A visual search was done to find plumes in the output component image set. However, once appropriate components were found, simply thresholding the component image was not sufficient to segment out only the plumes. Also, regions of energy being emitted or absorbed by the plume cannot directly be determined using this technique.

Spectral matched filtering was done for detection using atmospherically uncompensated imagery. An image mask was created from thresholded principal component output images, where all that was left was the extent or area of the plume. The mask was overlaid onto the scene to determine the section of the image used for the analysis. From this, on-and-off plume spectra were selected and were subtracted to create a

contrast spectrum. The contrast spectrum enhances the gas feature by removing the background influence. The atmosphere spectrum was merged with the target spectrum by multiplying the atmospheric transmission by the target spectrum on a wavelength-by-wavelength basis so that the data and the target spectrum appear to have been measured under the same conditions. The spectral matched filter application was done iteratively and resulted in a higher detection rate than SVD, including weak signal plumes and plumes that cover a small area.

Linear least-squares regression methods, unconstrained and constrained, were used to detect and quantify the plumes. Some methods used to generate basis sets for the regressions were: region of interest selection from the imagery, unsupervised classification, clustering techniques, and eigenvectors from the covariance matrix of the imagery.

In the discussion of endmember extraction, Young mentioned that thermal variation within the background is important. Specifically, when discussing extracted background spectra, Young wrote, “the signal is a direct thermal emission from the surface,” and that, “temperature variation over the scene becomes an important consideration.” Earlier it was mentioned that the thermal variation in the target would be neglected because, “the shapes of spectra are relatively insensitive to temperature,” and that, “detection analysis can be carried out with spectra for a fixed temperature.” It is because of this issue, that extraction methods do not explicitly accommodate for thermal variation, that endmember extraction was not used in the study[17].

The regression results showed that the constrained regression worked as well as the off-plume subtraction method, which had a high probability of detection. Unconstrained regression was not as successful and resulted in poor and incorrect results. Young determined this part of study was invalid because the result showed there was a negative contrast coefficient for water vapor. Unconstrained regression was unsuccessful because

the target gases were always found no matter if they were in the plume or not. Also, if a plume gas was not in the target set then there is no indication of this signature in the residual spectrum although it was in the plume. Essentially, if the algorithm looked for a specific gas it could find it even if the gas really was not present. If it did not specifically look for a gas, even if it was in the plume image, there would be no detection. In the constrained regression, the determination of whether a target gas should be included or excluded from the plume was done using the significance test, t-Test. This test evaluated the significance of change between regressions. The detection and quantification analysis was also done after pixels were grouped together to form a stronger signal. This procedure averaged out the absorption or emission characteristic of the signal.

The results of Young's study were that the spectral matched filter worked best for detection when the gases of interest were known and that constrained regression was optimal for detection and quantification.

Although Young did a robust study, there is still room for further research. Young had *a priori* knowledge of the gases that were in the scene. This work assumes nothing about the scene, not even if there is a plume present. Young mentioned that most of the gases in his study have spectral absorption coefficients that do not vary with temperature over the temperature range of interest (15 – 80°C). This research, in contrast to the Young study, utilized spectra measured at multiple temperatures for the target gases. These variations were shown previously in Figure 1.2. This work also utilizes the fact that the plume can be found in both emission and absorption.

2.3 Invariant Algorithms

Traditional matched filter detection converts a scene into reflectance by doing atmospheric compensation to look for a target which has a known reflectance. This assumes

that within the scene the surface is flat and there is a uniform atmosphere. This method is too generic for some scenes. The Healey-Invariant Algorithm was developed for material detection of a specific target spectrum within an image sensed under any illumination or atmospheric conditions[5]. It is used on non-atmospherically corrected hyperspectral data. The Healey-Invariant Algorithm converts the target into image space rather than the traditional detection method of converting the scene into target space. The target is converted into image space by incorporating the effects of the atmosphere and changing illumination conditions. These changes or variations, which are incorporated into the target spectra, are acquired by running a model with possible environmental parameter combinations that would potentially be present during the capture of an image, creating a target library. A set of basis vectors are then determined from this library which best represent the space filled by the spectral variations. An image pixel can then be tested by projecting it onto the basis vectors and if the error between the basis vector and the image pixel is below some threshold, then it can be classified as a target.

In Healey and Slater's (1999) implementation of the Invariant Algorithm, the variations in the known target spectra were modeled using various MODTRAN runs. The basis vector dimensionality was evaluated using SVD while the maximum likelihood classification determined how similar the image pixel was to the target[5]. When compared with an industry standard detection algorithm, Spectral Angle Mapper, the Invariant Algorithm had significantly fewer false detections.

Thai and Healey (2002) implemented a sub-pixel version of this algorithm for use on mixed-pixel situations. Due to spatial resolution constraints of most imaging systems, most pixel spectra represent a mixed-pixel. This implementation incorporated a target and a background subspace that were combined and compared to an image pixel. This algorithm was able to detect obscured targets with few false alarms. It also returned

better results than the widely used spectral matched filter[16].

Lee (2003)[8] developed an Invariant Algorithm that addressed the same problem as Thai and Healey for subpixel material identification without atmospheric compensation. This implementation, however, utilized a new method of generating basis vectors incorporating the maximum distance method (MaxD)[8] that results in orthogonal, linearly independent, basis vectors. This new method resulted in improved target detection. The maximum distance method assumes that the spectral library of interest is a subspace. By viewing the subspace in an n -dimensional form, the corners of the generated simplex that encloses the data are the points that are the maximum Euclidean distance from any point within the simplex as described in Figure 2.2. These points are found by first determining the vector at the most extreme point from the origin and that closest to the origin, as shown in Figure 2.2a, these points are now considered corners of the simplex. The difference vector is found between these two vectors, as shown in Figure 2.2b. Then a hyperplane perpendicular to the difference vector is determined, as shown in Figure 2.2c. The data points can then be projected onto this plane, as shown in Figure 2.2d. This process is repeated, until all the data points are collapsed onto one point. As the process is repeated each extrema are then considered to be the basis vectors, as shown in Figure 2.2e. The linear combinations of those basis vectors will recreate all the data contained within the simplex[8]. A subset of these basis vectors will be used for the target basis vectors; again this is done to save time otherwise all basis vectors could be used for testing.

The implementations of the invariant algorithm presented above were applied to the gas detection and identification problem and the effectiveness was evaluated as part of this research.

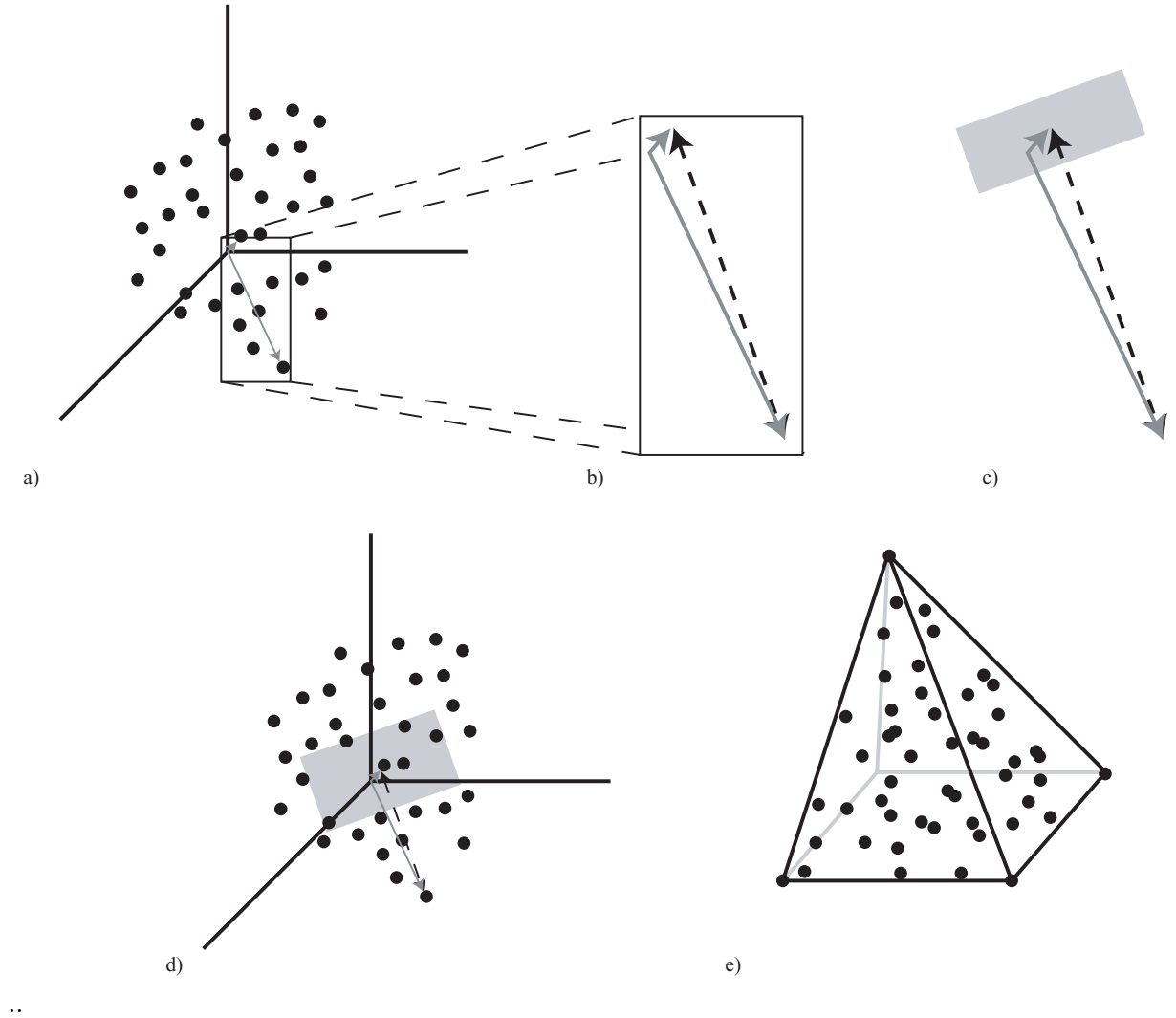


Figure 2.2: a) The vectors are showing the points furthest from the origin and closest to the origin. b) The dotted vector represents the difference vector. c) A plane is found perpendicular to the difference vector. d) The data can then be projected onto the new plane. e) This n -dimensional representation of the data shows the basis vectors at the corners of the simplex

2.4 Algorithm Applicability

The invariant algorithm was developed to do target detection in scenes having varying atmospheric and illumination conditions. The original application of these invariant algorithms solved for a target under various atmospheric and illumination conditions in the visible, near-infrared and short-wave infrared regions of the electromagnetic spectrum. Gases have properties such as transparency and emission or absorption that cannot be removed from an image which is why traditional matched filter is not ideal for this application. The invariant algorithm is applicable to the gas problem because the signatures need to be detectable no matter what the conditions are, *i.e.*, concentration, temperature, mixture ratios, etc. Specifically, as stated by Clausen and Bak (1998), the gas concentration can be determined if the following parameters are known or measured: the background temperature or spectrum, gas temperature, path length, and the absorption spectrum at the gas temperature [2]. These are all the parameters that were considered when describing the invariant space for gas identification and detection.

The invariant algorithm as applied in this work was quite different from Healey and Lee's application because the effluent gas targets have features in the LWIR and are optically thin causing them to be transparent and, at times, even invisible. The problem was further complicated because the plume can be in emission and absorption. An example of a situation where this would arise is near to the stack where the plume is hot and downwind the plume has had a chance to cool. The plume could cool to a temperature less than the background temperature which may be solar heated, so photons emitted from the background are then absorbed by the plume before they reach the sensor. Another problem is that the plume temperature and concentration are unevenly distributed along a given vertical slice or column within the plume. The target spectrum looks different at different temperatures as well as different concentrations.

The background characteristics will significantly influence the resultant pixel spectrum and may be more prominent than the gas targets. This causes the pixel spectrum to always be mixed regardless of the sensor's ground resolution.

Chapter 3

Approach

3.1 Radiance Model

This research concentrated on the self-emitted photons from a gaseous plume target, path f , as shown in Figure 3.1. This radiant energy is referred to as L_{plume} . The self-emitted background photons, forming path g , are all the surface photons that are not the target, referred to as L_{ground} . The paths h and i represent the self-emitted target radiance reflected off the background and the downwelled radiance respectively; these paths are neglected because of the near-unit emissivity assumed for the background. Finally, the upwelled radiance path, j , gives the self-emission of the atmosphere between the target and the sensor or L_{atm} . The total sensor reaching radiance is

$$L_{total} = \tau_{atm}(L_{ground} \cdot \tau_{plume} + L_{plume}) + L_{atm}, \quad (3.1)$$

where

$$\begin{aligned} L_{total} &\equiv \text{total radiance } \left[\frac{W}{cm^2 sr \mu m}\right] \\ L_{ground} &\equiv \text{Planckian radiance at the temperature of the ground} \end{aligned}$$

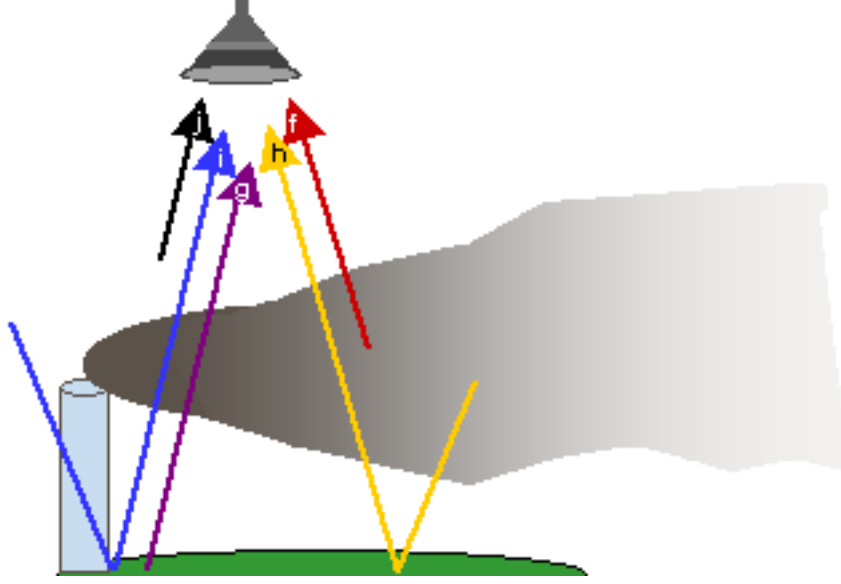


Figure 3.1: The self-emitted energy paths are: f) self-emitted, g) background self-emitted, h) self-emitted reflected by background, i) downwelled, j) upwelled.

$\tau_{plume} \equiv$ transmission through the plume

$L_{plume} \equiv$ Planckian radiance at the temperature of the plume

$\tau_{atm} \equiv$ transmission through the atmosphere

$L_{atm} \equiv$ upwelled radiance of the atmosphere.

The Planckian blackbody radiance of an object at a specific temperature is given by

$$L_{planck} = \frac{2hc^2}{\lambda^5(e^{\frac{hc}{\lambda kT}} - 1)}, \quad (3.2)$$

where

$h \equiv$ Planck's constant = $6.6256 \cdot 10^{-34} [J \cdot s]$

$c \equiv$ speed of light = $2.9979 \cdot 10^8 \left[\frac{m}{s} \right]$

$\lambda \equiv$ wavelength [m]

$$\begin{aligned}\kappa &\equiv \text{Boltzmann gas constant} = 1.38 \cdot 10^{23} \left[\frac{J}{s} \right] \\ T &\equiv \text{temperature [K]}.\end{aligned}$$

The transmission of the plume τ can further be described as

$$\tau_{plume} = 1 - ck(\lambda), \quad (3.3)$$

where c is the concentration path length $[ppm \cdot m]$ or the number density of the gas multiplied by the path length, and $k [\frac{1}{ppm \cdot m}]$ is the absorption spectrum of the gas. The equation is derived from Beer's Law and is described in the next section.

3.1.1 Beer's Law

Beer's law defines the transmission, τ , as

$$\tau = e^{-ck} \quad (3.4)$$

where the concentration path length is c , and the absorption spectrum is k . In conditions where there is a small optical depth or an optically thin plume, *i.e.* where $ck \ll 1$ a Taylor-series expansion can be done that reduces the equation to

$$\tau = 1 - ck. \quad (3.5)$$

Ultimately, one would like to work in terms of emissivity rather than transmission. Transmission and emissivity are related in Kirchhoff's Law as

$$\tau + \epsilon + r = 1, \quad (3.6)$$

where r , the reflectance. The reflectance, or in this case the scattering, can be ignored because the plume is assumed to be non-scattering in the LWIR. The particles in the plume are small compared to the wavelength of interest, therefore, Rayleigh scattering applies. Rayleigh scattering is modeled as

$$\beta_r(\lambda, \theta) = \frac{2\pi^2}{m\lambda^4} (n(\lambda) - 1)^2 (1 + \cos^2\theta), \quad (3.7)$$

where $\beta_r(\lambda)$ is the angular scattering coefficient, m is the number density, θ is the angular direction of scattering relative to direction of propagation, and $n(\lambda)$ is the index of refraction of the medium. This equation shows that the scattering is dominated by $\frac{1}{\lambda^4}$. Since this work concentrates on the LWIR region of the spectrum, the scattering contribution is negligible.

Rearranging Equation 3.6 gives

$$\epsilon = 1 - \tau. \quad (3.8)$$

Substituting Equation 3.5 into Equation 3.8 gives

$$\epsilon = ck, \quad (3.9)$$

confirming the description of τ in Equation 3.3.

3.2 Description of the Invariant Target Space

The target space for the plume was described in terms of the radiance model as shown in Figure 3.2. This representation is called the single slab model. In this discussion the term slab refers to a homogenous mass that has a consistent temperature and concentration throughout. The mathematical representation for this is described in Equation 3.1. The atmospheric terms, τ_{atm} and L_{atm} , implemented were estimated

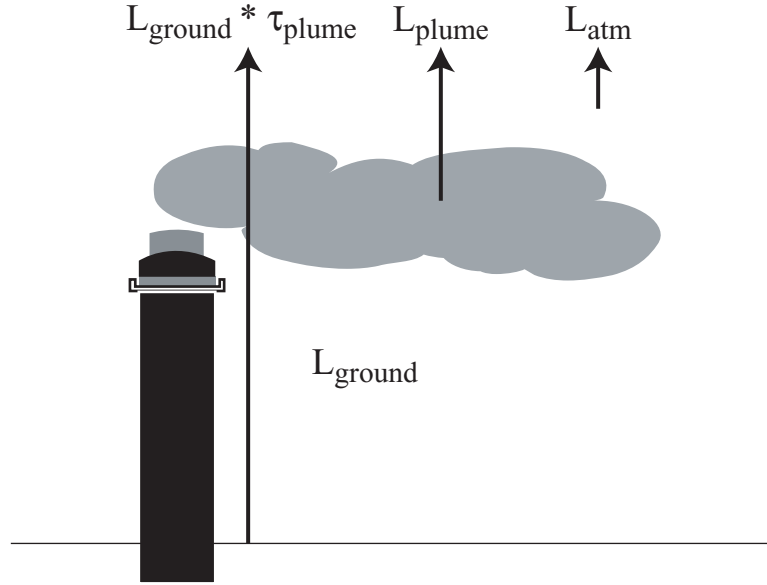


Figure 3.2: This represents the radiance model that will be used to describe this problem.

using a mid-latitude summer atmosphere MODTRAN[14] simulation. For the purpose of this research the τ_{atm} and the L_{atm} terms will be held constant, and are shown in Figures 3.3 and 3.4 respectively. In the traditional implementation of the invariant algorithm these terms are varied. A more appropriate description of the plume radiance would be in terms of the multiple slab model, as represented in Figure 3.5, because the plume itself is a varying body. The plume can be described by a normally distributed temperature and concentration profile across the plume (Figure 3.6) and following an exponential decay in the quantities downwind. The multiple slab model better represents this variation. The primary advantage of the multiple slab model over the single slab model is that it can represent whether the plume is in emission or absorption in its entirety. When tracing a line between the ground and the sky or the ground and the sensor, the plume constituents are not constant along this path. The differences in the radiance equation between the two slab models are the $L_{m,\text{plume}}$ and $\tau_{m,\text{plume}}$

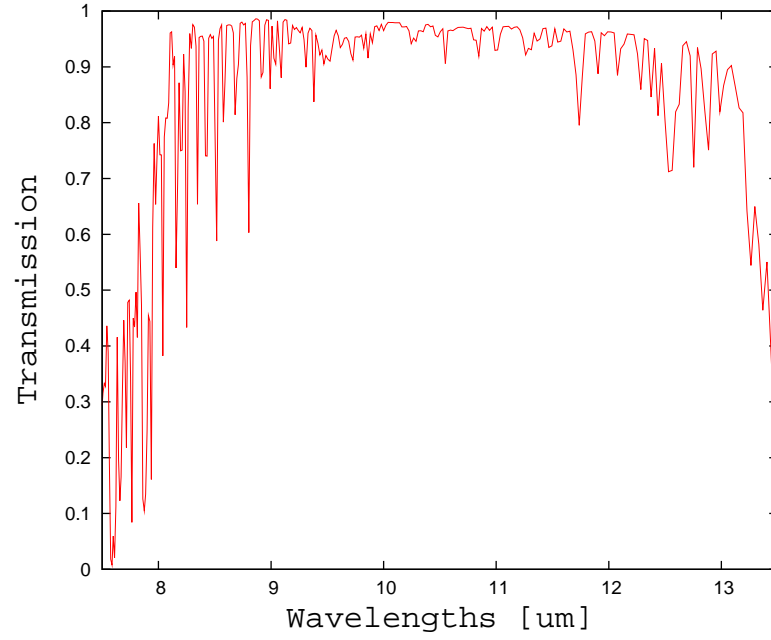


Figure 3.3: Atmospheric transmission used in this study

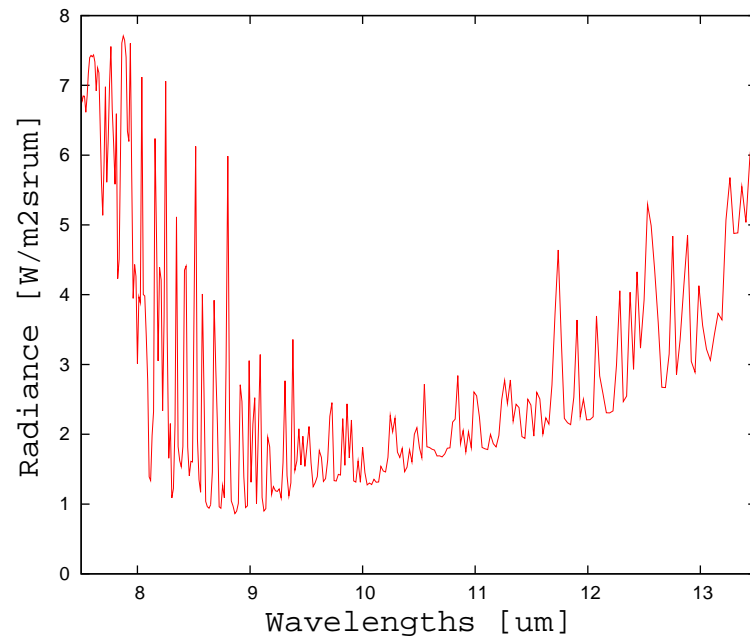


Figure 3.4: Atmospheric radiance used in this study

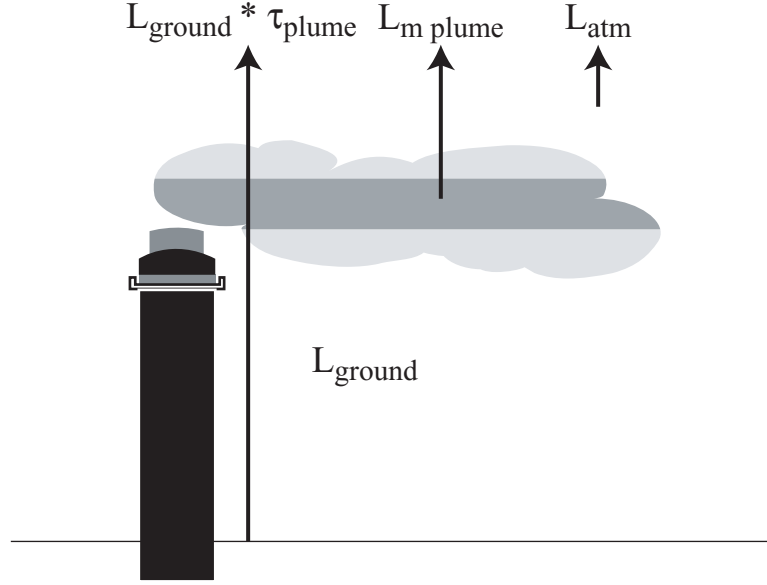


Figure 3.5: This represents the column effects, where the different layers represent the varying parameters of the plume.

terms, which are:

$$L_{m,total} = \tau_{atm}(L_{ground}\tau_{m,plume} + L_{m,plume}) + L_{atm} \quad (3.10)$$

$$\tau_{m,plume} = \prod_i^N \tau_i \quad (3.11)$$

$$\tau_i = 1 - c_i k \quad (3.12)$$

$$L_{m,plume} = c_N k L_{planck}(\lambda, T_N) + \sum_{i=1}^{N-1} \left[\prod_{j=i+1}^{N-1} \tau_j c_i k L_{planck}(\lambda, T_i) \right]. \quad (3.13)$$

The $L_{m,plume}$ term becomes the summation of the concentration in the i th layer times the absorption spectrum multiplied by the Planckian radiance at the temperature of

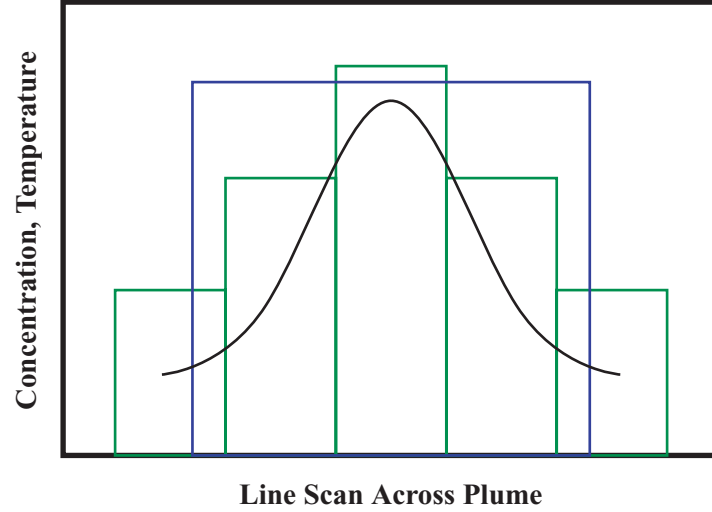


Figure 3.6: Simplification of the Gaussian plume model (smooth curve); for the single slab (single rect) and multi-slab (multiple rects) cases.

the plume in that layer. The transmission through the plume, $\tau_{m,plume}$, becomes the product of the transmission, τ_i , in the N constituent layers where the transmission of the i th layer is one minus the concentration of the gas in the i th layer times the absorption spectrum. The multiple slab model is not used in this work and is presented only for completeness. The plume itself is generated by varying the species of gas, concentration, and gas temperature. These permutations describe the target space used in this research.

3.3 Test Data

All test scenes used in this research were generated using a physics-based synthetic image generation environment, DIRSIG[7], which uses first-principles physics to model a scene. This simulation environment allows scenes to be generated along with corresponding truth maps. Some examples of the truth maps are: temperature of each pixel in the image (plume, background, etc.) as well as concentration of the gas species.

These scenes have highly varying, complex backgrounds composed of trees, buildings, grass and asphalt parking lots as shown in Figure 3.7. The sensor model that was used to generate these simulated scenes was similar to the SEBASS[3] instrument. The noise added to the modeled system mimics that of the SEBASS sensor and is spectrally correlated; meaning that from band to band the noise is dependent. The noise covariance image is shown in Figure 3.8 and was created from the SEBASS spectrally correlated noise cube[12]. The plume simulation model used in DIRSIG is the Jet Propulsion Lab (JPL) plume model[4], which implements a Gaussian concentration and temperature distribution orthogonal to the downwind direction and an exponential decrease of these quantities downwind. This simulation results in a full three-dimensional model of a plume. The DIRSIG rendering of the plume generated by the JPL model is considered to be spectrally accurate, however, the spatial fidelity is considered weak. This is not an issue for this work because the algorithm works on a pixel-by-pixel or spectral basis.

3.3.1 Plume Emission and Absorption Implementation

This work exploited the difference between the plume temperature and the background temperature, ΔT . The plume temperature was described in terms of the surface temperature, $T_{surface}$, and an offset of the surface temperature, ΔT , as shown in Figure 3.9. This offset term is both positive and negative, which represented the plume in emission and absorption, respectively. A surface temperature of $36^{\circ}C$ was used for this research. This is the mean scene derived brightness temperature for the test scene, not including the plume. The concentration and temperature ranges for gas spectra for the target subspace were generated between 1-1000 ppm-m and $\pm 15^{\circ}C$ from the derived surface temperature. The gas absorption spectra that this study utilized were chosen from the list of the top hazardous gases according to the EPA's Clean Air Act. The laboratory absorption spectra for each gas, taken from a commercially available database, were



Figure 3.7: A band at $10.73 \mu\text{m}$ from the test scene that was used.

measured at three temperatures. The laboratory spectrum used varied with the plume temperature. The laboratory spectrum that was selected was that which was measured at the temperature that was closest to the temperature of the plume.

3.4 Basis Vectors

There are various means to determine basis vectors from a set of n -dimensional data. This research looked at two methods; SVD and MaxD from the Healey and Lee algorithms, respectively. The most rigorous part of this work was the generation of the spectral libraries used to select target basis vectors using the previously stated radiometric model. The spectral libraries were generated for each gas at each temperature

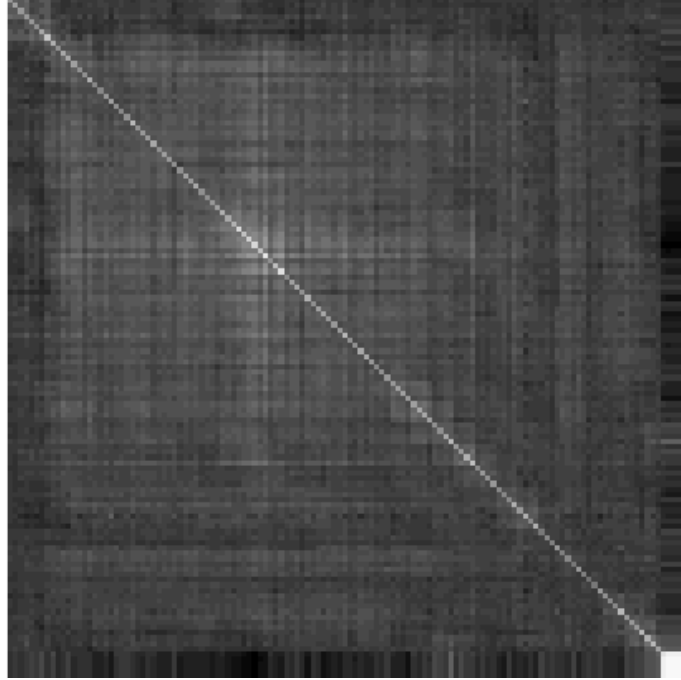


Figure 3.8: SEBASS noise covariance image.

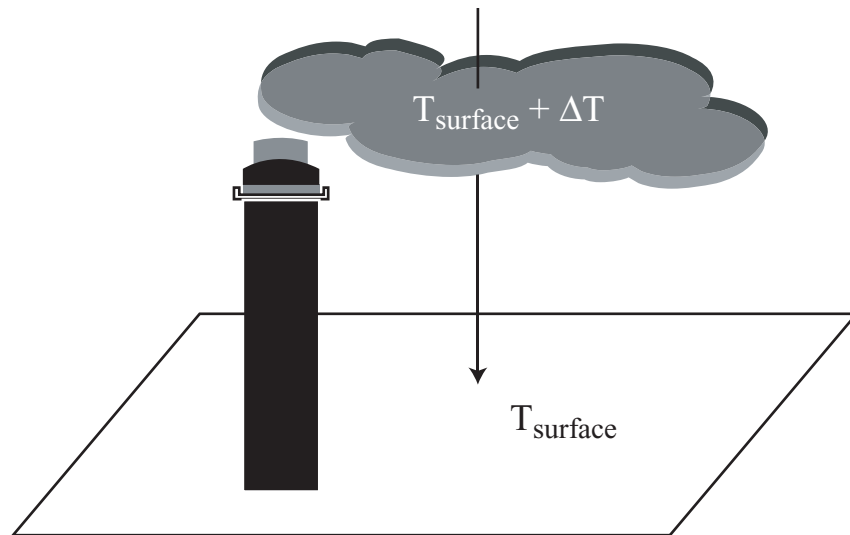


Figure 3.9: The temperature of the plume can be represented by the surface temperature plus some offset.

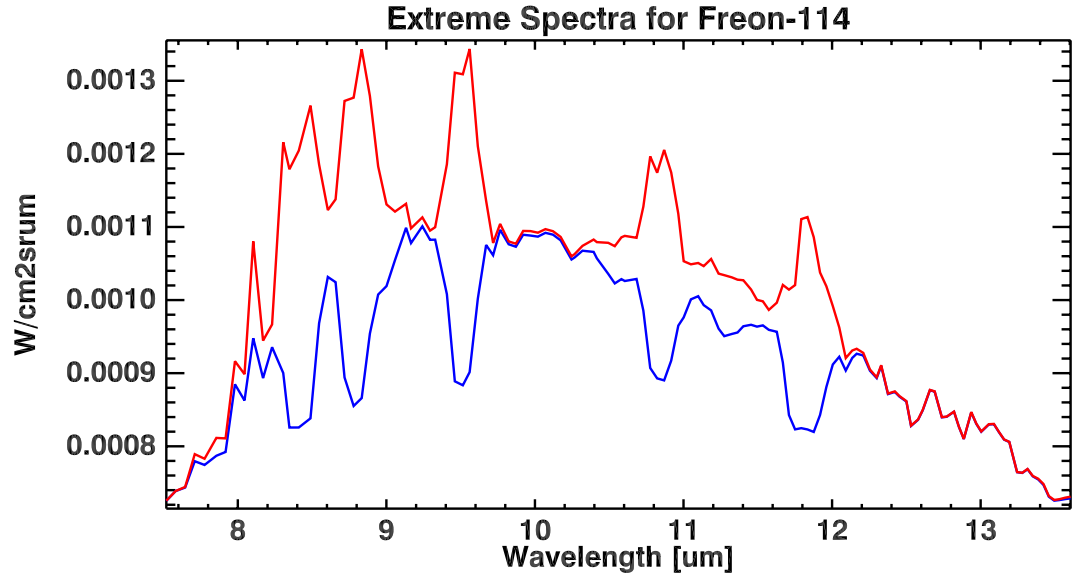


Figure 3.10: The extremes of the Freon-114 target spectral library. The top spectrum shows the target gas in emission, while the bottom is in absorption.

and concentration combination. The library is built having spectra in absorption and emission. The extremes for Freon-114 are shown in Figure 3.10. A set of ten target basis vectors were selected for each gas, an example of these are shown in Figures 3.11 and 3.12. The basis vectors from SVD shown here have more structure than the MaxD. SVD basis vectors have been rotated into a new space where as MaxD are actual spectra and when plotted offset much of the structure is compressed. Background basis vectors were derived from a synthetically generated test scene without the plumes included. An example of these are shown in Figures 3.13 and 3.14. When using real imagery, a region of interest in an area within the scene, where there was no plume present as to not include the target as part of the background, should be used in order to obtain background basis vectors. There were 15 basis vectors selected to describe the background.

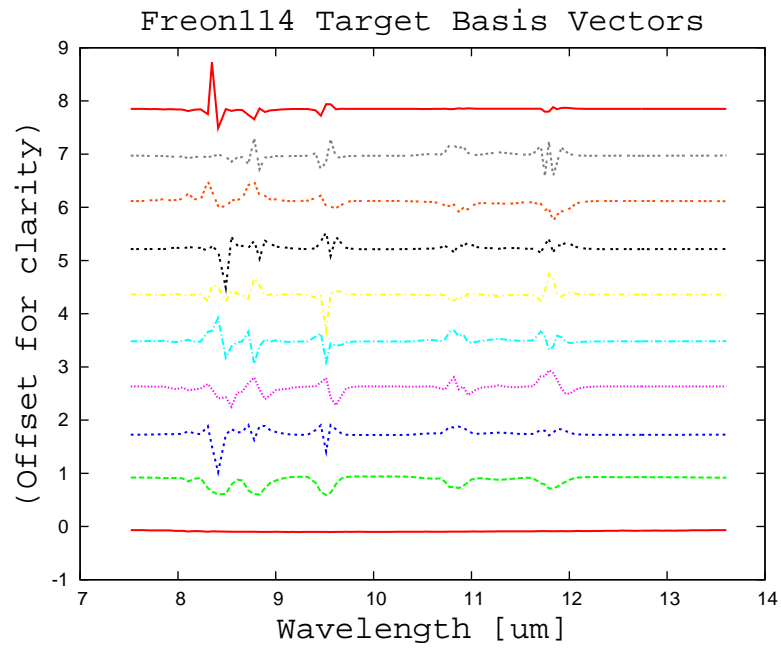


Figure 3.11: The top 10 target basis vectors, which were used in this study, for Freon-114 as defined by SVD and determined from a target library of nine temperatures and eight concentrations. (Note: The structure in the first basis vector is not seen; it was compressed due to the other offset plots.)

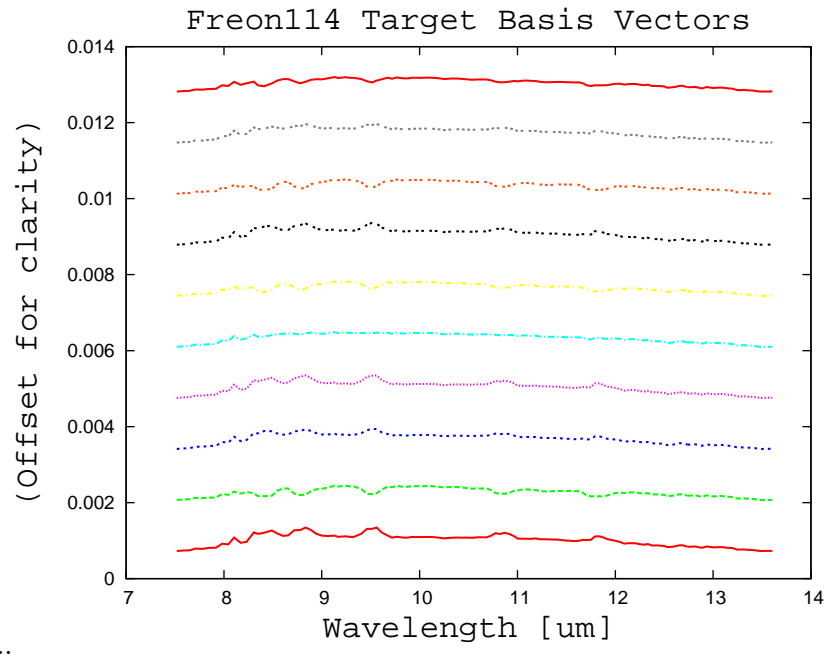


Figure 3.12: The top 10 target basis vectors, which were used in this study, for Freon-114 as defined by MaxD and determined from a target library of nine temperatures and eight concentrations.

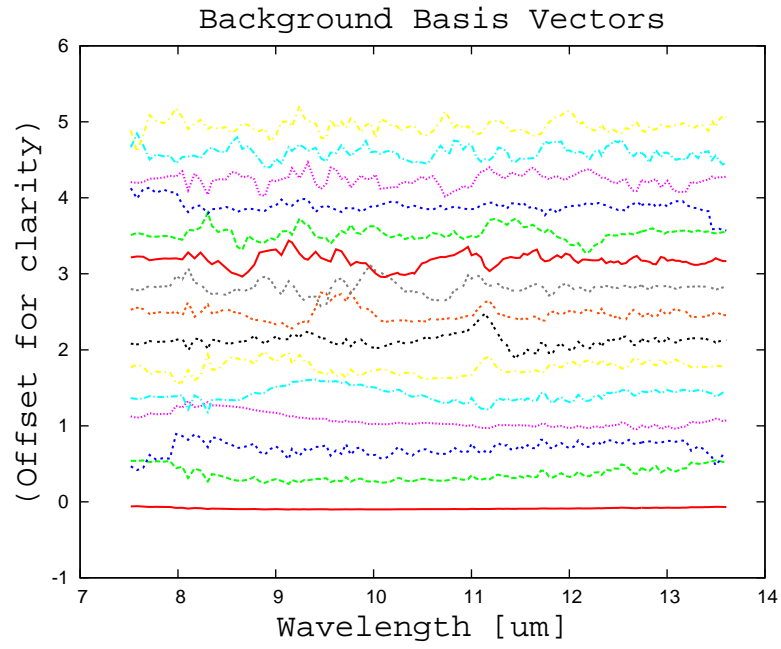


Figure 3.13: The top 15 background basis vectors, which were used in this study, for the background as defined by SVD. (Note: The structure in the first basis vector is not seen; it was compressed due to the other offset plots.)

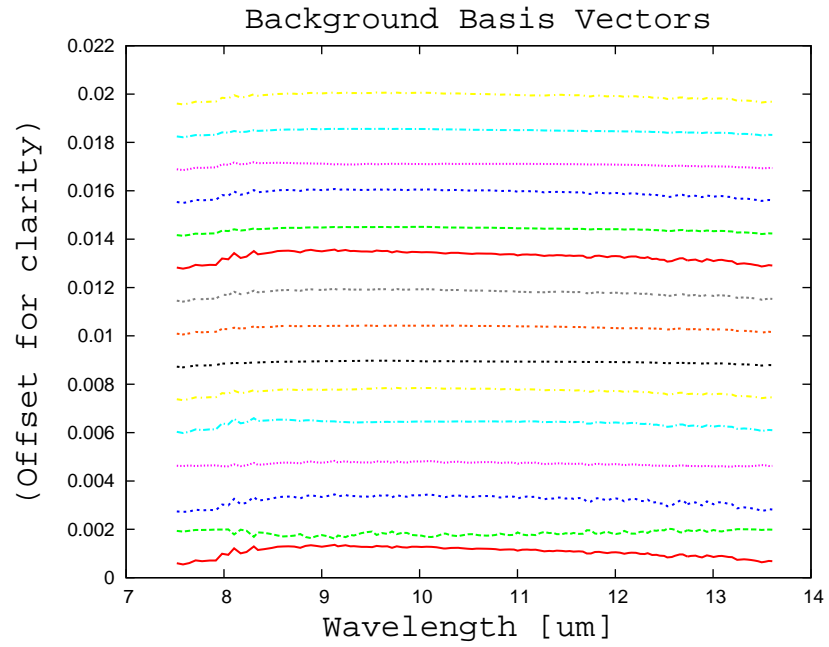


Figure 3.14: The top 15 background basis vectors, which were used in this study, for the background as defined by MaxD.

Chapter 4

Results

4.1 Analysis

The effectiveness of the algorithms employed by this research were tested against DIRSIG scenes having the same background scene elements but different plume configurations. The scenarios tested were as follows in Table 4.1. Each scene was exploited using a reduced set of target and basis vectors using two methods; SVD and MaxD. Seven uniquely constructed target signature libraries were reduced by each method and then used to process the images. These spectral libraries were built using different

Table 4.1: This shows test scenarios that were used in this work.

Scene Reference	Plume #	Gases	Release Rate (g/s)
Case 2	2	Ammonia, Freon-114	50
Case 4	2	Ammonia, Freon-114	0.25
Case 5	1	Ammonia, 1,1,2,2-Tetrachloroethane	0.25
Case 6	2	Methane, 1,2-Dichloropropane	0.25
Case 7	2	Fluorobenzene, Phosgene	0.25, 0.50

Table 4.2: Varying temperatures and concentrations used to build the test signature libraries.

Name	# Temperatures	# Concentrations	Combinations
T5C5	5	5	25
T6C8	6	8	48
T7C9	7	9	63
T8C8	8	8	64
T9C8	9	8	72
T10C8	10	8	80
T14C8	14	8	112

combinations of gas temperatures and concentrations. These different combinations are shown in Table 4.2.

The generalized likelihood ratio test (GLRT) was applied to each scenario to determine the likelihood of finding the test gas in each pixel. The algorithm was run so that a result map was output for each gas as a third-dimension or “band” of a detection map cube. Table 4.3 describes the structure of the detection cube.

Each pixel’s GLRT response was normalized by the process followed by equations 4.1–4.3.

$$\mathbf{G} = [g_1, g_2, \dots, g_N] \quad (4.1)$$

$$d = \sqrt{\sum_i^N g_i^2} \quad (4.2)$$

$$\mathbf{G}' = \frac{\mathbf{G}}{d} \quad (4.3)$$

A pixel here is described as vector \mathbf{G} comprised of g_i GLRT responses for the N gases and the normalized pixel is \mathbf{G}' . This forces the algorithm, in a sense, to choose which gas it is claiming is most likely in the pixel. These normalized GLRT detection maps

Table 4.3: Index of gases as they correspond to the third dimension or “bands” of the output GLRT detection map cube.

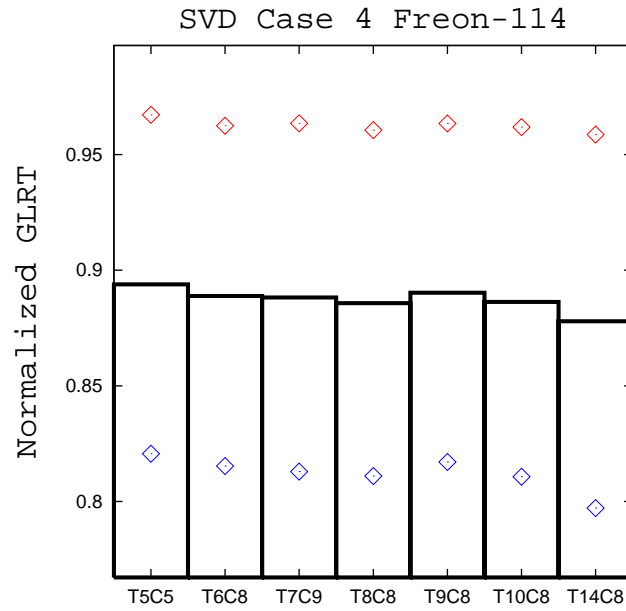
Band Index	Gas	Band Index	Gas
1	Acrolien	15	Freon-125
2	Fluorobenzene	16	Freon-12
3	Benzene	17	Freon-134a
4	Carbon tetrachloride	18	Freon-218
5	Methyl chloride	19	Formaldehyde
6	Methane	20	Hydrogen chloride
7	Carbon dioxide	21	Ammonia
8	Carbon monoxide	22	Phosgene
9	Dichloromethane	23	Sulfur hexafluoride
10	1,2-Dichloropropane	24	Sulfur dioxide
11	1,3-Dichloropropane	25	1,1,2,2-Tetrachloroethane
12	1,2-Dibromomethane	26	Trichloroethylene
13	1,2-Dichloromethane	27	Vinyl chloride
14	Freon-114		

are evaluated in two ways. For each scene a region of interest (ROI) was determined over a small portion of the plume near the stack. The mean value for each gas over the ROI was determined. These mean values are then plotted as a detection profile where the band index on the horizontal axis corresponds to a unique gas in the library. The detection map corresponding to the gas in each release was visually inspected to be sure that the detected pixels “looked” spatially like a plume. The normalized GLRT detection map as well as the mean ROI detection profile are the two figures that will be presented to demonstrate the utility of the algorithms.

4.2 Library Size

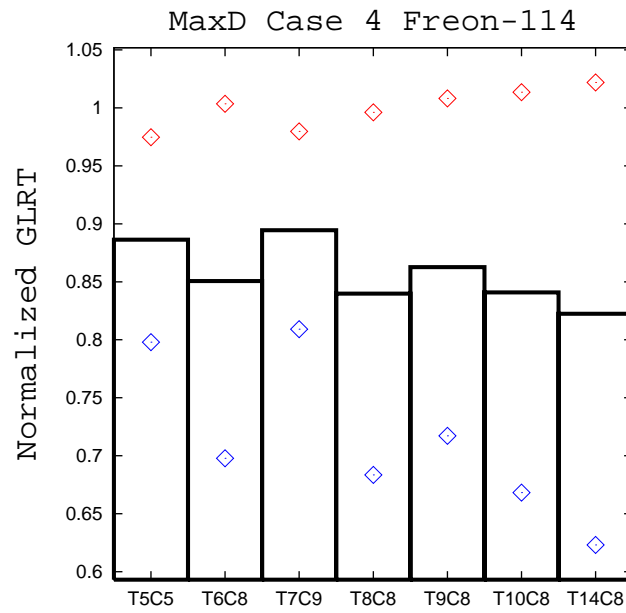
This research evaluated the best size for the target spectral library. These libraries, as described in Table 4.2, were reduced taking 10 target basis vectors and 15 background basis vectors using both SVD and MaxD for basis vector selection. It should be noted that the range of temperatures and concentrations were also the same for all libraries. The temperatures and concentrations used to generate the library are uniformly spaced over the range of each of these parameters. The results shown in this section are from Case 4, which had two single gas plumes of ammonia and Freon-114, and the ammonia results from Case 5. These scenarios were selected for this study because they were neither the worst nor the best detections of all the cases; they provided a moderate challenge. Cases 4 and 5 have a gas in common (ammonia), which is released at the same rate. Case 5 is a multiple gas release (one plume) in contrast to the two single gas plumes in Case 4.

The mean detection metric over the ROI for each gas of interest was plotted in order of increasing size of the library to determine which returned the highest detection. Figure 4.1 shows that for the Case 4 Freon-114 plume, using SVD, the smallest spectral library, T5C5, gave the best results. The worst results were produced from using T14C8, the



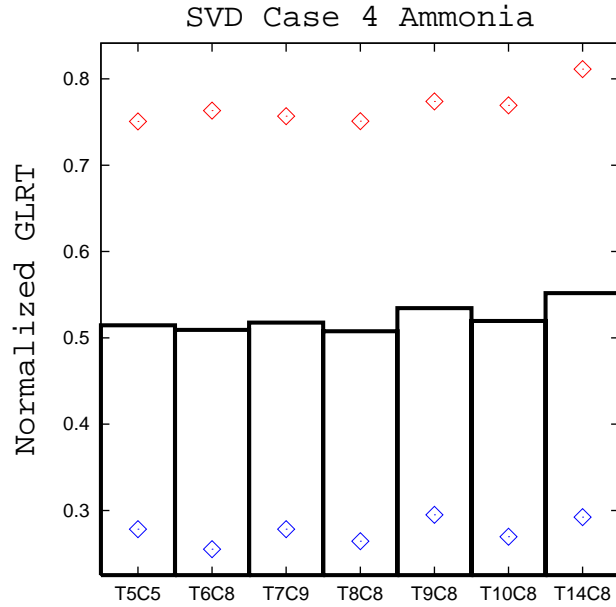
..

Figure 4.1: Case 4, Freon-114 band results using SVD for each of the libraries, where the indices correspond to the libraries as listed in Table 4.2. The points represent the standard deviation.



..

Figure 4.2: Case 4, Freon-114 band results using MaxD for each of the libraries, where the points represent the standard deviation.

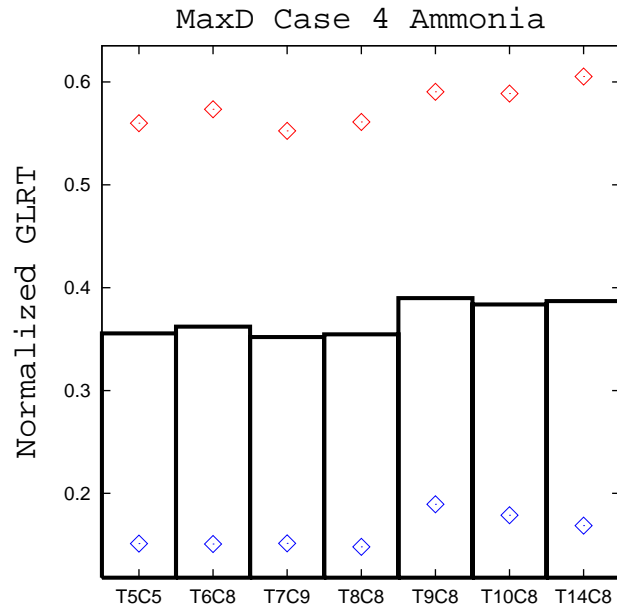


..

Figure 4.3: Case 4, ammonia band results using SVD for each of the libraries, where the points represent the standard deviation.

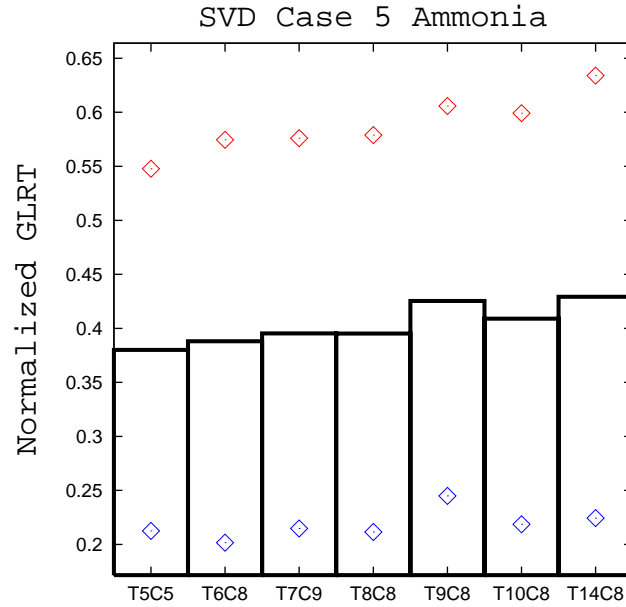
largest target spectral library. The MaxD Case 4 Freon-114 plume results, shown in Figure 4.2, are different although the worst detection again was returned by T14C8. The best detection was returned from T7C9. More remarkable is how the the libraries differentiate one from the next more so than was seen in the SVD results for this plume. This could be driven by how the basis vectors were selected. For example, looking at T8C8 and T9C8 for both SVD and MaxD respectively, there is a much more distinguished difference for the MaxD results while the libraries only differ by one spectrum. One spectrum would influence MaxD more than SVD because it is a geometric method for generating basis vectors rather than statistical (SVD).

Figures 4.3 and 4.4 show the results for the ammonia plume for Case 4, and have different results than the Freon-114 plume. Here for the SVD case the largest spectral library, T14C8, showed the best results, while T8C8 showed the worst results. The



..

Figure 4.4: Case 4, ammonia band results using MaxD for each of the libraries, where the points represent the standard deviation.

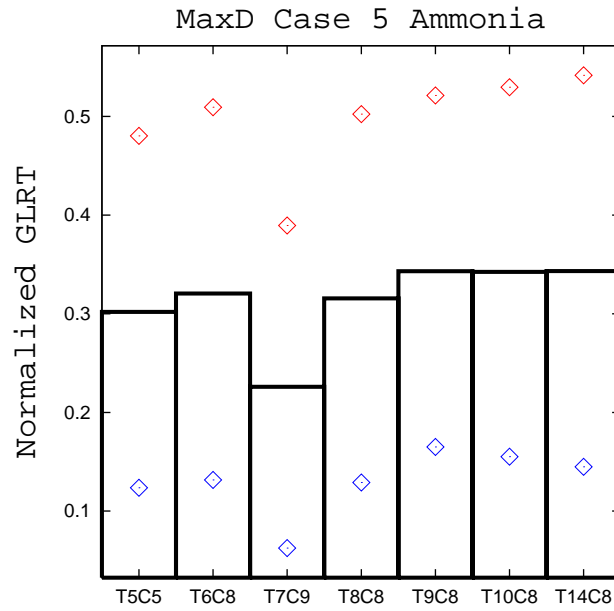


..

Figure 4.5: Case 5, ammonia band results using SVD for each of the libraries, where the points represent the standard deviation.

MaxD results are again very different from the SVD case and have the best results with the T9C8 library and worst with the T7C9 library.

The Case 5 ammonia results were examined in Figures 4.5 and 4.6. The smallest library, using SVD, returned the worst results. The top detection for this case using SVD was the largest library, T14C8. While this is the same as the SVD Case 4 ammonia detection it was only slightly larger than the T9C8 library and the trend does not follow for all the libraries. The MaxD results for the ammonia in Case 5 show the worst detection from T7C9. There are equal detections between T9C8, T10C8, and T14C8 which is the highest return value. Taking a closer look at the data the three sets are the same to the third significant digit where T10C8 returns the lowest of the three values and then the other two are the same to the fourth significant digit where T14C8 shows



..

Figure 4.6: Case 5, ammonia band results using MaxD for each of the libraries, where the points represent the standard deviation.

a slightly higher value than T9C8.

Ultimately, there does not seem to be an optimum size for the library for either basis vector selection method. There were libraries which were better than others, however, it could be said that they all work equally well. Two statistical tests were implemented on the data to try and show that the means of the data shown here were the same. The first was the two tailed t-Test[11]; this failed because this test assumes that the data is normally distributed, which it is not. The Mann-Whitney test[1] was also implemented. However, this also failed because it assumes that each data set has the same distribution, which they do not. Considering no library distinguished itself as giving the best detections and the fact that T9C8 is a library that was shown to be one of the best detectors in each case, the remainder of this analysis will look only at the results from the library T9C8.

4.3 SVD vs. MaxD

Another objective of this work was to determine which basis vector selection method, SVD or MaxD, provided better results. This study was done using Case two, which showed two strong single plume releases of Freon-114 and ammonia. Figures 4.7 and 4.8 show the detection maps for both SVD and MaxD for the Freon-114 band. From both of these scenes it is evident that both methods, SVD and MaxD, detect the Freon-114. While SVD appears to do better job at suppressing the background, MaxD has more/stronger detections in the Freon-114 plume region. Also, looking at the detection profile for the Freon-114 plume for both SVD and MaxD, in Figures 4.9 and 4.10 respectively, they both show Freon-114 as the most likely gas in the plume region with very high probability.

The second release in Case 2 is the ammonia plume which was also detected by both of these methods as shown in Figures 4.11 and 4.12. The results for the ammonia

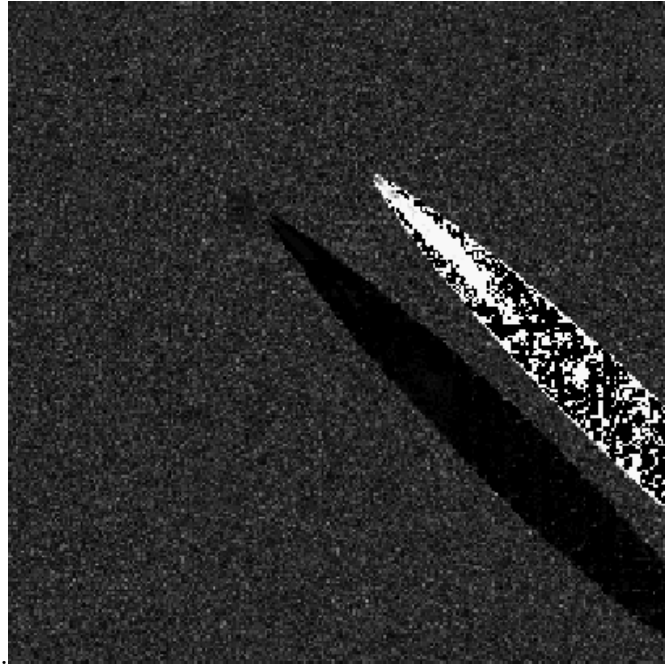


Figure 4.7: Normalized GLRT results for the Freon-114 band, which used SVD for basis vector selection.

plume using both basis vector selection methods are shown quite dramatically and more thoroughly than the Freon-114 plume. Again, SVD looks to a better job with background suppression. However, for the MaxD ammonia map the background is suppressed more than it was in the MaxD Freon-114 map. This indicates that for ammonia using the MaxD basis vectors the GLRT was more “convinced” that the background was not ammonia than Freon-114. This is promising since ammonia is an atmospheric gas and it could be found in the atmosphere above the background. The SVD and MaxD detection profiles for the ammonia plume region are shown in Figures 4.13 and 4.14, respectively. These show that SVD has a slightly higher detection for the ammonia than MaxD. The MaxD results also show higher detection values than SVD for gases that are not in the plume region. The gas sulfur hexafluoride (index 23) also stands out in both the SVD and MaxD case; this will be discussed later in this

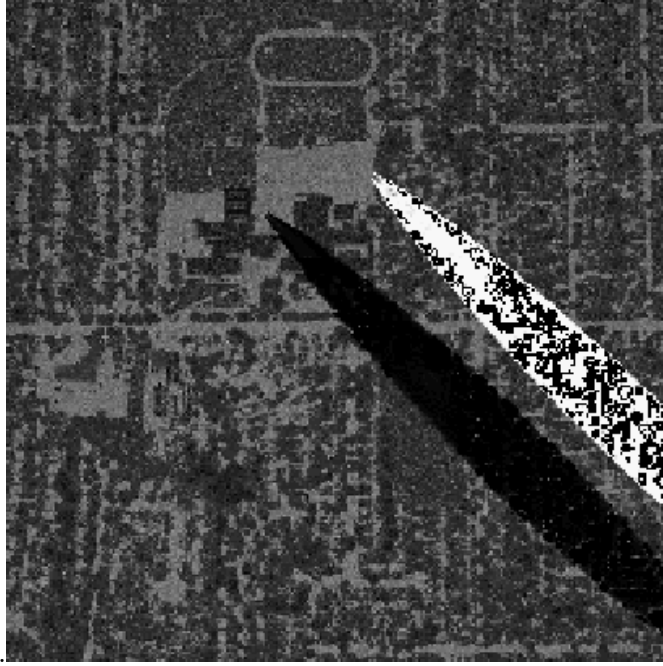


Figure 4.8: Normalized GLRT results for the Freon-114 band, which used MaxD for basis vector selection.

document.

These results show that SVD does a slightly better job overall. This being said, as before, the scale at which the basis vector selection methods are being evaluated at are on par with each other and either are appropriate for gas detection and identification. Due to this, and for conciseness, the rest of this document will present only those results from the SVD implementation.

4.4 Case 4

The rest of the document will discuss the results from specific cases as listed in Table 4.1, beginning with Case 4. This case is a weak release of only 0.25 g/s. This scene is the same as Case 2, which was discussed in the previous section except for the release

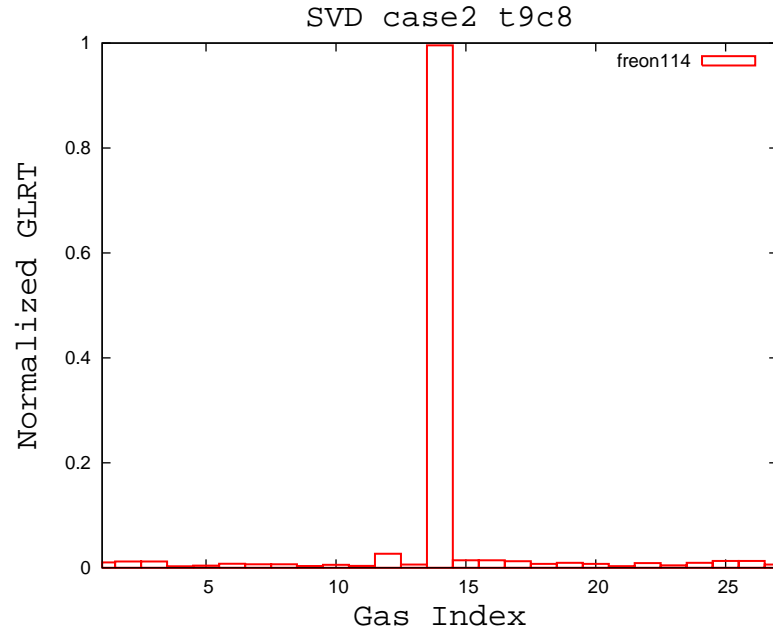


Figure 4.9: Detection profile for the Freon-114 plume region, which used SVD for basis vector selection.

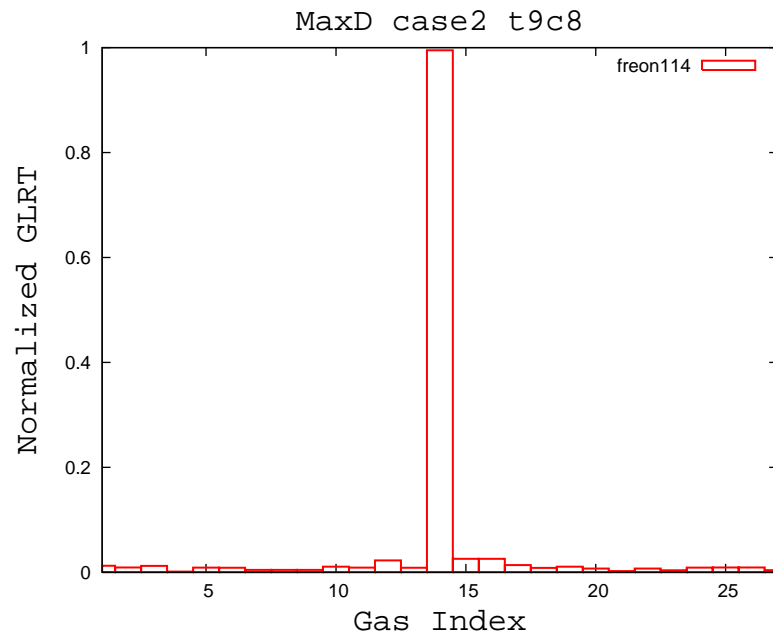


Figure 4.10: Detection profile for the Freon-114 plume region, which used MaxD for basis vector selection.

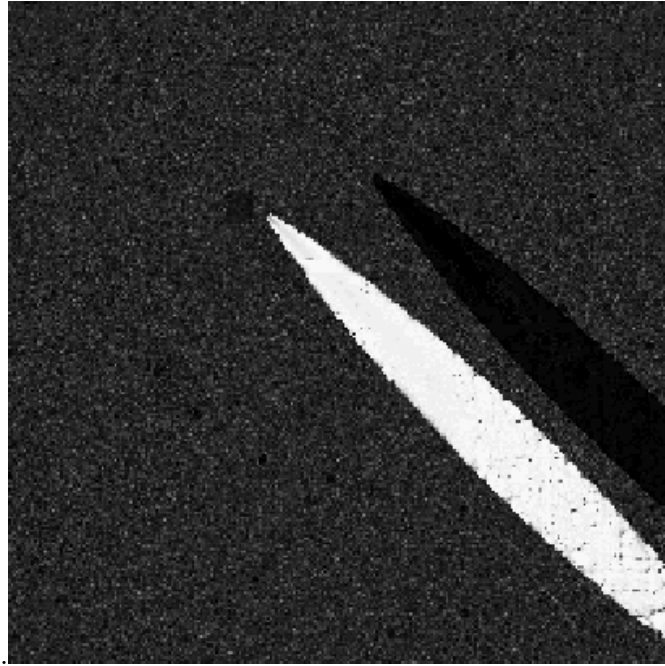


Figure 4.11: Normalized GLRT results for the ammonia band of Case 2, which used SVD for basis vector selection.

rate. Case 4 has a release rate that is significantly less than Case 2, which is considered a strong release.

The Freon-114 plume again was detected well as is shown by the detection map in Figure 4.15. This illustrates that the algorithm is detecting the plume at downwind positions but that there are background materials beneath the plume that seem to suppress detection more than others. The algorithm detects to a concentration of about 1 ppm-m. In this scene the algorithm seems to do well matching against the trees and not as well with the rest of the background materials. This demonstrates that the background basis vectors are doing a “good job” matching target pixel. This is not completely unexpected since in a weak release the signature from the gas is going to be weaker and less differentiable from the background. This should not overshadow the fact that it is detecting against all background materials, just that it is doing better

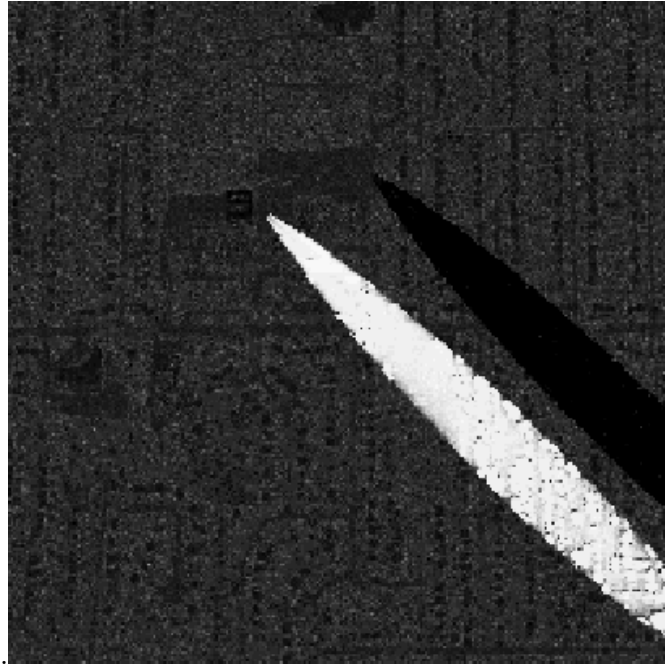


Figure 4.12: Normalized GLRT results for the ammonia band of Case 2, which used MaxD for basis vector selection.

against the trees. The detection profile for this plume region, as seen in Figure 4.16, shows a very high probability for the Freon-114 band (band 14).

The utility of the detection profile is that the user should not have to look at all of the gas detection maps of the image to determine which gas is in the plume. The detection probability spectrum allows the user to simply look at the detection maps displaying a high value in the detection profile. Once the user looks at those detection maps which gave high probabilities, the next thing to do, to determine if there is a plume in the scene, is to evaluate whether there is “plume structure” in the map. Following this process for the second plume of Case 4, the detection profile shown in Figure 4.17 is examined.

The highest probabilities in the profile are for ammonia (band 21) and SF_6 (band 23).

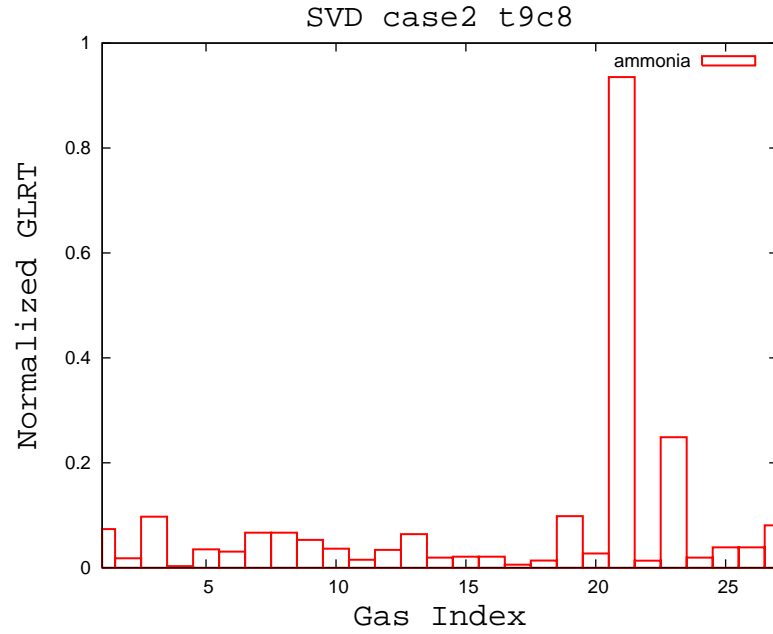


Figure 4.13: Detection profile for the ammonia plume region of Case 2, which used SVD for basis vector selection.

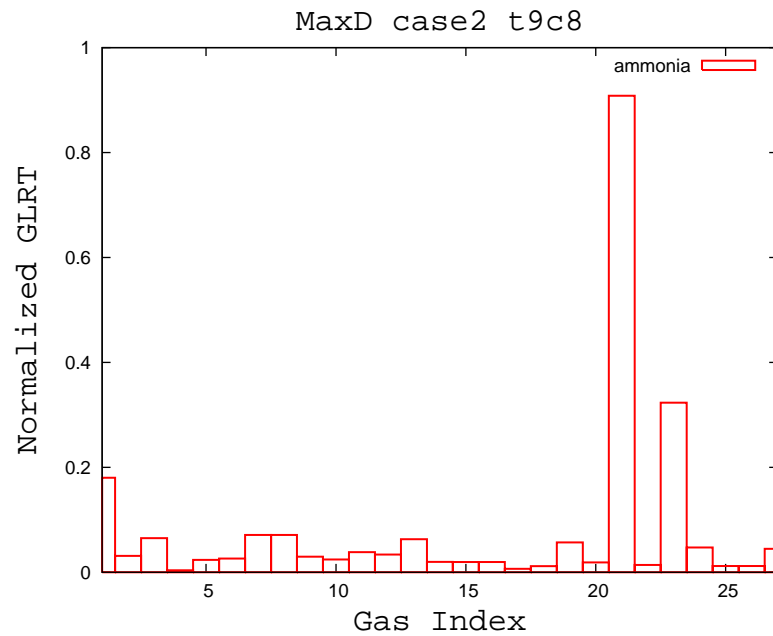


Figure 4.14: Detection profile for the ammonia plume region of Case 2, which used MaxD for basis vector selection.

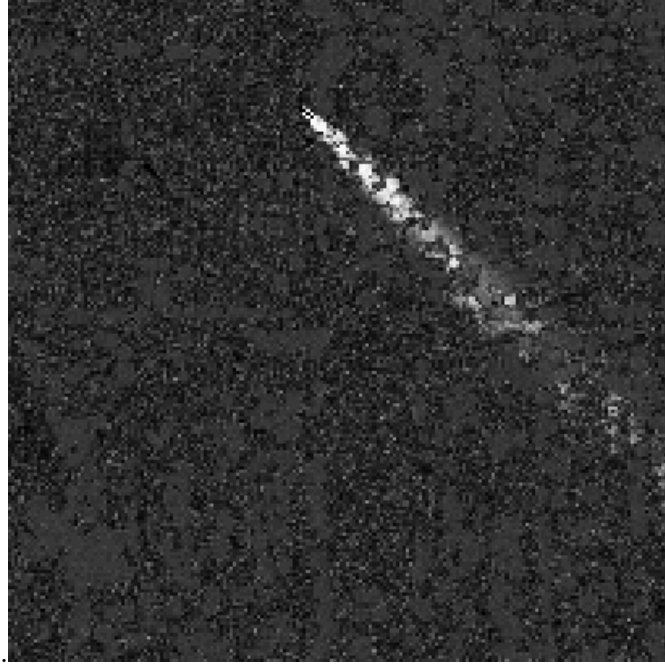


Figure 4.15: Normalized GLRT results for the Freon-114 band of Case 4, a weak release.

The ammonia detection map, Figure 4.18, shows a high (bright) return close to the stack and weaker detections downwind, about 4 ppm-m, but ultimately it is important to see that there is plume structure exhibited. In the SF_6 detection map, Figure 4.19, there are not bright returns that show plume structure.

4.4.1 Atmospheric Mismatch

A question that arises when doing gas identification and detection is how well does the atmosphere in the radiance model have to match that of the test scene. For this study the percent of the gas in the total atmospheric column, which is below the sensor for a particular atmospheric gas is on average 38.4%, as shown in Table 4.4.

This study showed if there is a different atmosphere in the test scene than was implemented in the radiance model, the algorithm still proves applicable for gas detection

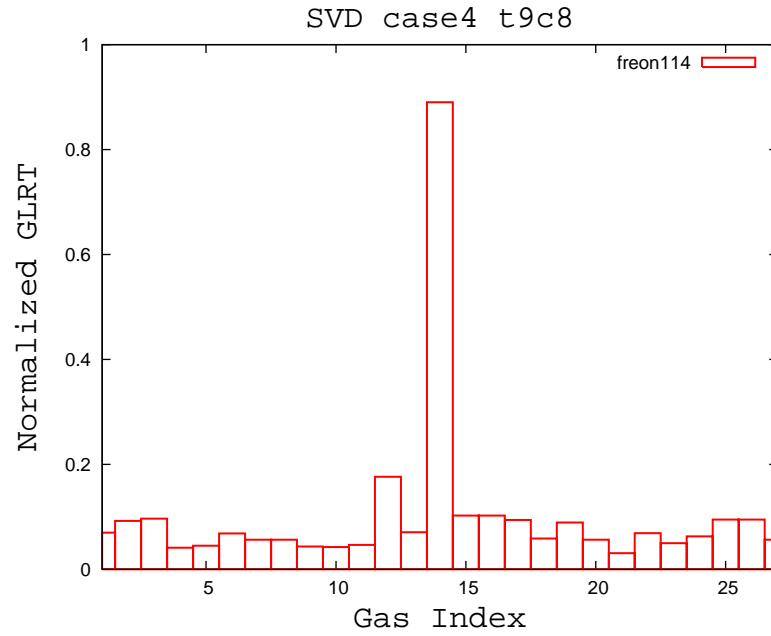


Figure 4.16: Detection profile for the Freon-114 plume region of Case 4, a weak release.

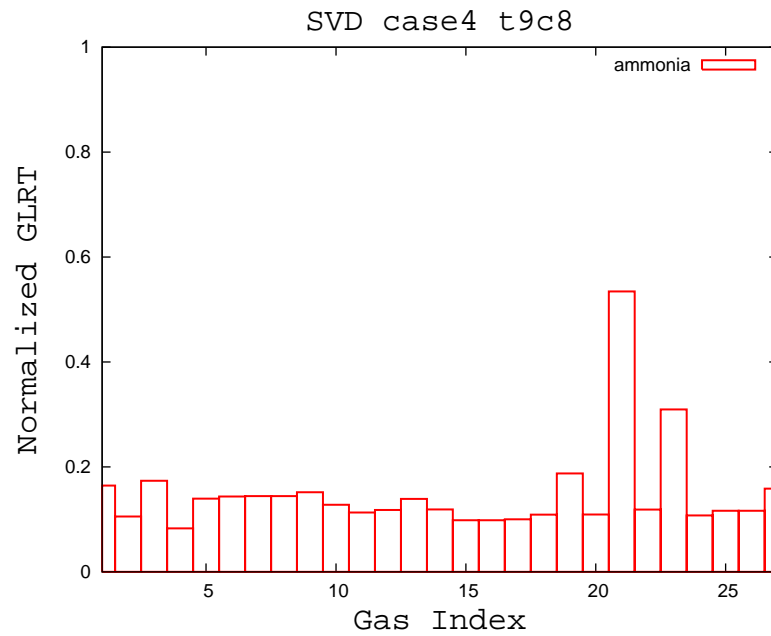


Figure 4.17: Detection profile for the ammonia plume region of Case 4, a weak release.

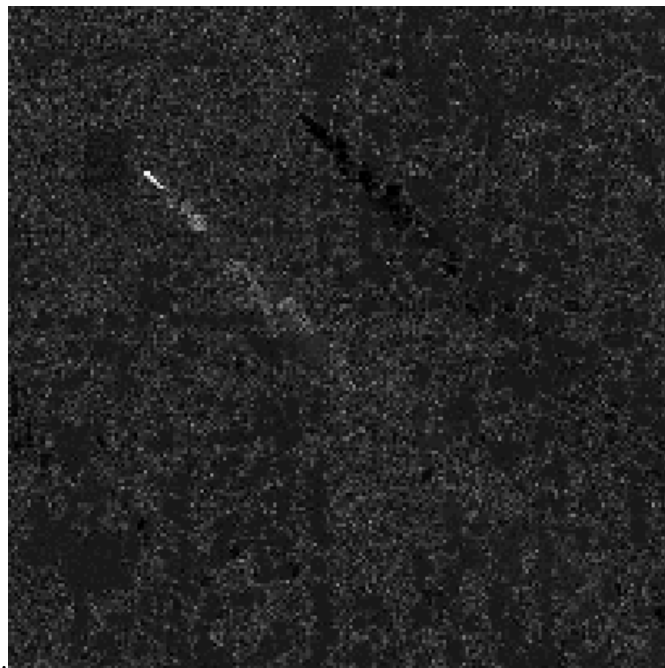


Figure 4.18: Normalized GLRT results for the ammonia band of Case 4, a weak release.

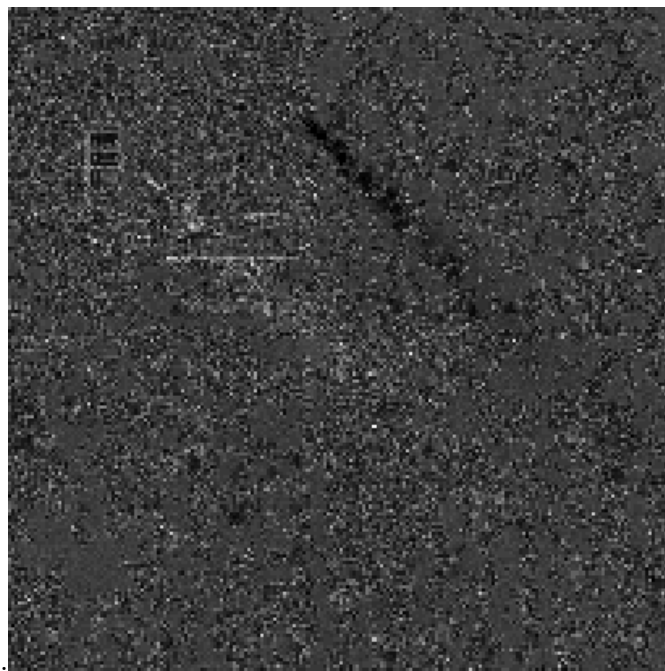


Figure 4.19: Normalized GLRT results for the SF_6 band of Case 4, a weak release.

Table 4.4: The percent of the primary atmospheric gases in the total atmospheric column below the sensor, which is at 1000 feet.

Atmospheric constituent	% Captured in test scene
Water	73
Ozone	16
Carbon dioxide	31
Carbon monoxide	35
Methane	32
Nitrous oxide	32
Oxygen	31
Ammonia	57
Nitrogen monoxide	31
Nitrogen dioxide	31
Sulfur dioxide	53

and identification. Figures 4.20 and 4.21 show the detection probability spectra for the Freon-114 and ammonia plumes, but in this implementation of the target model, the atmospheric properties were changed. This target model used atmospheric parameters from a Moderate Resolution Transmittance: atmospheric model (MODTRAN) mid-latitude winter (rather than mid-latitude summer which was the atmosphere used in the scene). The results are quite similar to those with atmospheric properties which match the scene presented in the previous section. In fact, they appear to have the same probability of detection for both of the gases which are in each plume. The similarity is also seen in the detection maps as shown in Figures 4.22 and 4.23.

To further emphasize this point the algorithm was run using a target library including no atmospheric contributions at all. These results, seen in Figures 4.24 and 4.25, are again very similar to those already presented. Of the detection profiles shown here, the ammonia case is the most important. Ammonia is an atmospheric gas and of the total ammonia in the atmospheric column 57% of it is below the sensor and captured in the

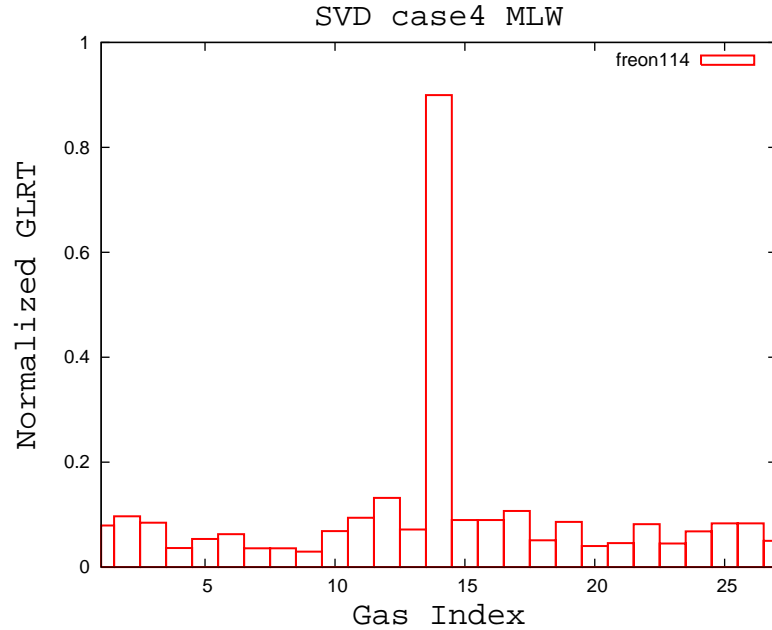


Figure 4.20: Detection profile for the Freon-114 plume region of Case 4, a weak release, using target spectra with an atmosphere that does not match that of the scene.

test scene. This study shows that including atmosphere in the target model does not significantly effect target detectability for the cases studied here.

4.5 Case 7

Case 7 is similar to the previous Case 4 except that in this scene there are two new gases to be detected, which are released at different rates. The first gas, fluorobenzene, was released at the same rate as those in Case 4, 0.25 g/s. The probability profile is shown in Figure 4.26. This figure shows that band 2, fluorobenzene, has the highest probability with no other gases worth investigating. This is further supported by the fluorobenzene detection map showing very strong detections in the region of this release, Figure 4.27. It has the same background issues as the other case, however, the algorithm is still detecting the plume; near the stack as well as downwind.

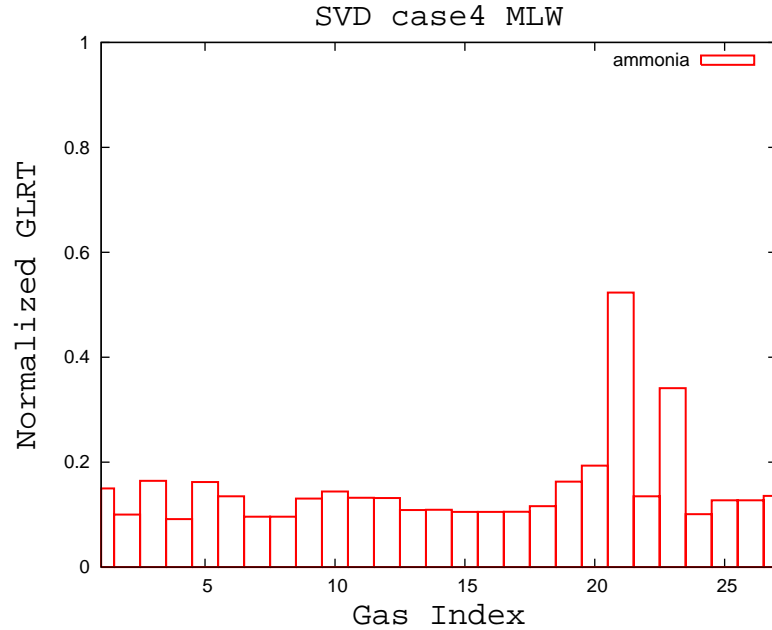


Figure 4.21: Detection profile for the ammonia plume region of Case 4, a weak release, using target spectra with an atmosphere that does not match that of the scene.

The next plume releases phosgene at a rate of 0.5 g/s, twice as much as was released in Case 4. The detection profile, Figure 4.28, again shows a strong detection for the gas being released, phosgene (band 22), with no other gases having a strong probability of being in the plume. The detection map for this gas, Figure 4.29, shows that it is a much larger plume than the other in the scene. It still has the same background issues but is detecting throughout the spatial extent of the plume.

4.6 Case 5

There are two gases released in the same plume in Case 5. These gases, ammonia and 1,1,2,2-tetrachloroethane, are being released at the same rate of 0.25 g/s. In the detection profile, Figure 4.30, the top two returns are from bands 21 and 25. The band with the highest probability of being a plume gas is ammonia, band 21, which

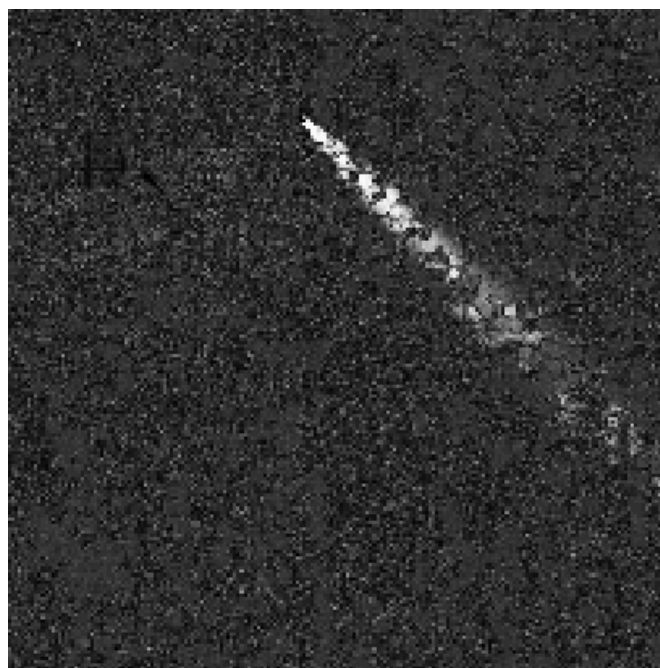


Figure 4.22: Normalized GLRT results for the Freon-114 band of Case 4, a weak release, using target spectra with an atmosphere that does not match that of the scene.

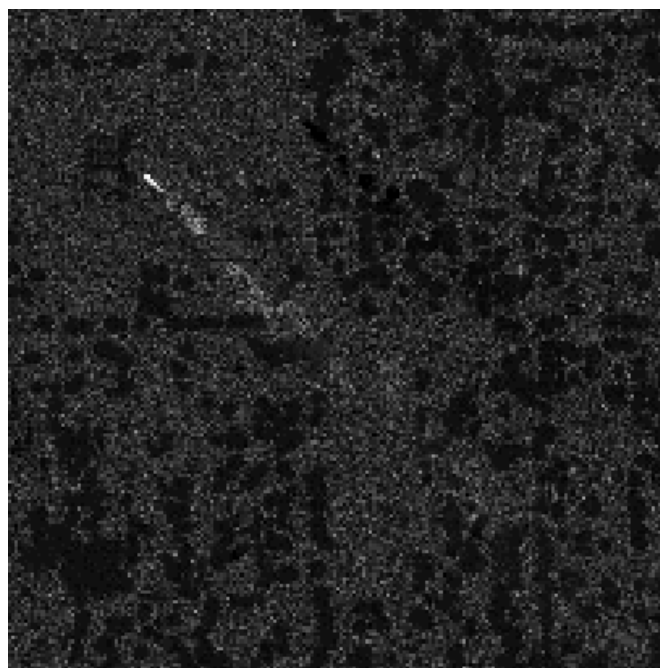


Figure 4.23: Normalized GLRT results for the ammonia band of Case 4, a weak release, using target spectra with an atmosphere that does not match that of the scene.

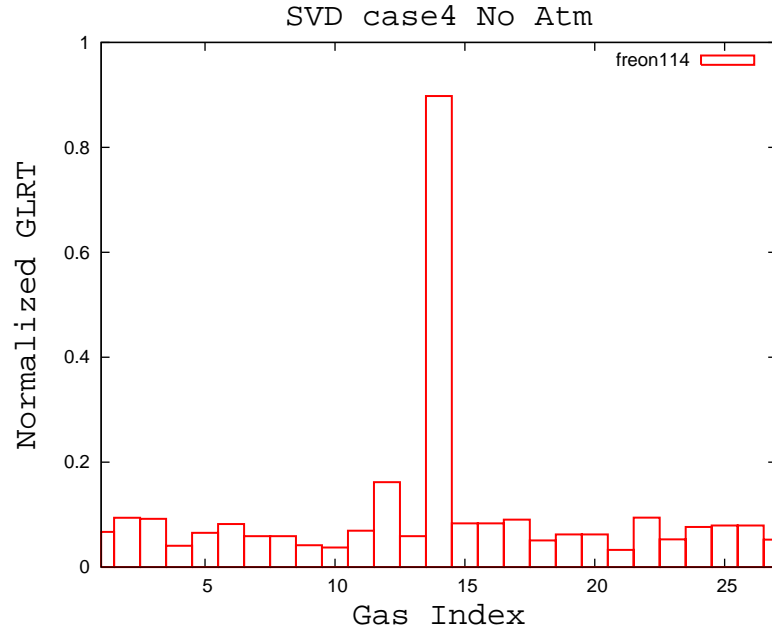


Figure 4.24: Detection profile for the ammonia plume region of Case 4, a weak release, using target spectra which do not incorporate atmospheric parameters.

is supported by the distribution of pixels shown in Figure 4.31. The detection map for 1,1,2,2-tetrachloroethane, band 25, is shown in Figure 4.32. The plume structure, although subtle, is evident which demonstrates a positive detection. The raw absorption spectrum for 1,1,2,2-tetrachloroethane, Figure 4.33, shows strong features to detect off of. However, once put through the radiance model which converts it into target spectra, 1,1,2,2-tetrachloroethane has lost much of its discerning features as seen in Figure 4.34. This is because the features are on the edge of the atmospheric transmission window, which explains lesser plume structure in the detection map.

4.7 Case 6

The last scene for evaluation is Case 6. This scene has two single gas weak releases of 1,2-dichloropropane and methane at 0.25 g/s. The results for 1,2-dichloropropane are shown

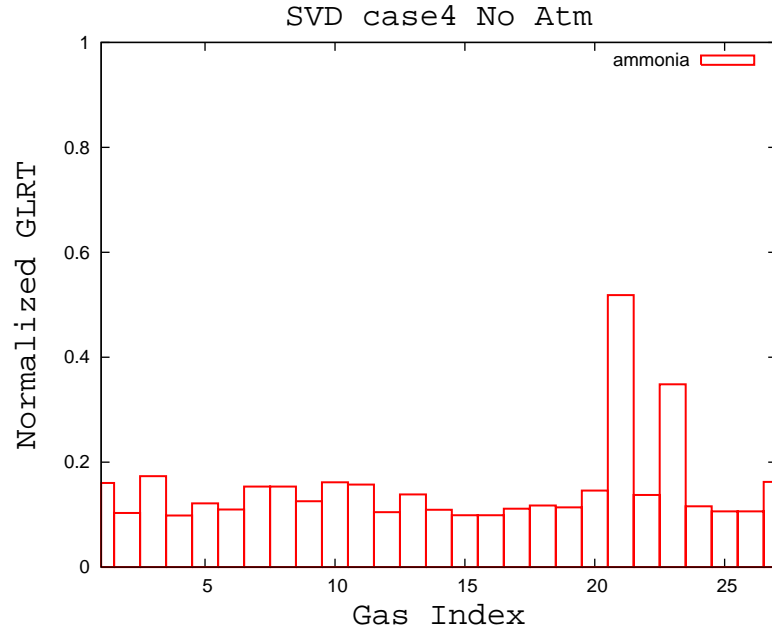


Figure 4.25: Detection profile for the ammonia plume region of Case 4, a weak release, using target spectra which do not incorporate atmospheric parameters.

in Figures 4.35 and 4.36. Although the detection band does not exhibit as large of a plume structure as previously seen, it is very evident that band 10, 1,2-dichloropropane, stands out from any other gases in the detection profile. The other plume does not return as promising of a result, as seen by the detection profile, Figure 4.37. Band 6 methane has the highest probability, although, it is only slightly higher than the rest. More importantly the detection map, Figure 4.38 does not show the plume structure; although there is a bright pixel at the location of the release. Again, the atmosphere is the culprit for these poor results. The spectrum for methane, Figure 4.39, shows it to only have features on the edge of the atmospheric transmission window where the transmission is quickly falling in value. Investigating the image very closely, there is a bright pixel by the stack which is a detection. The results are not as pronounced as shown before, however, the algorithm is still detecting accurately.

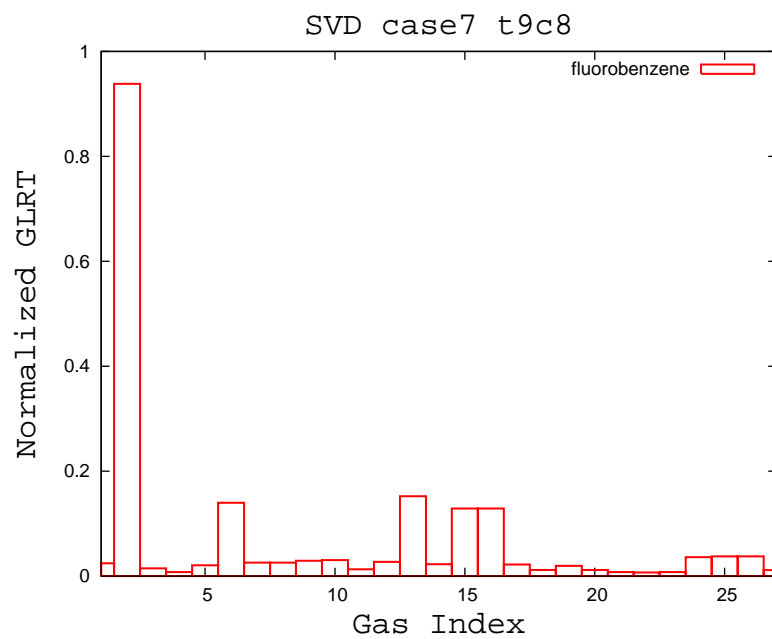


Figure 4.26: Detection profile for fluorobenzene the plume region of Case 7, a weak release.

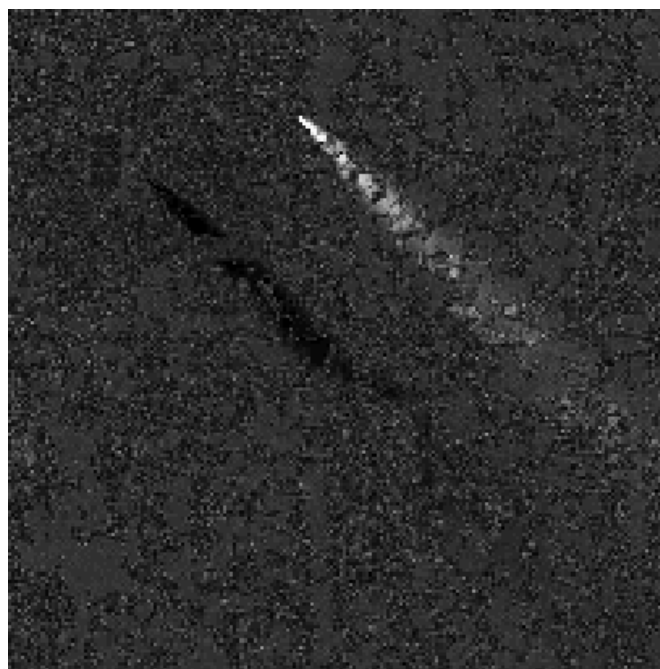


Figure 4.27: Normalized GLRT results for the fluorobenzene band of Case 7, a weak release.

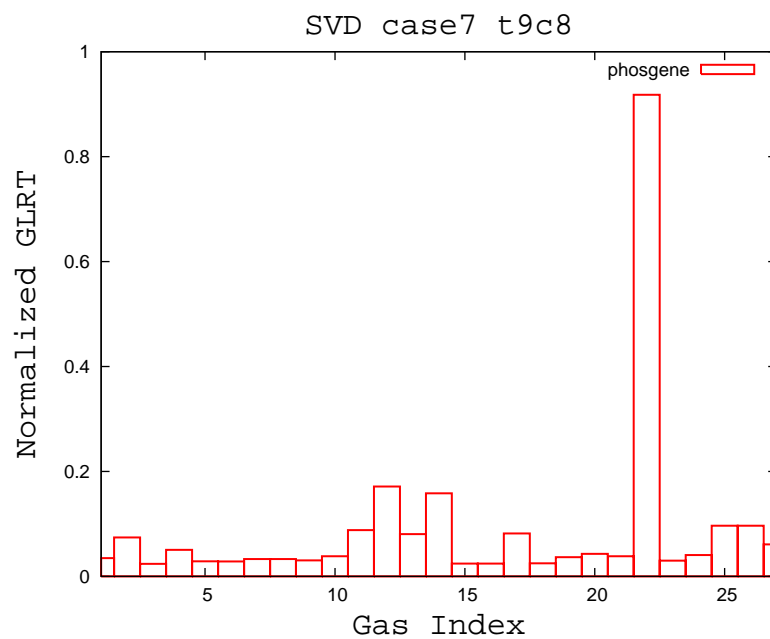


Figure 4.28: Detection profile for the phosgene plume region of Case 7, a weak release.

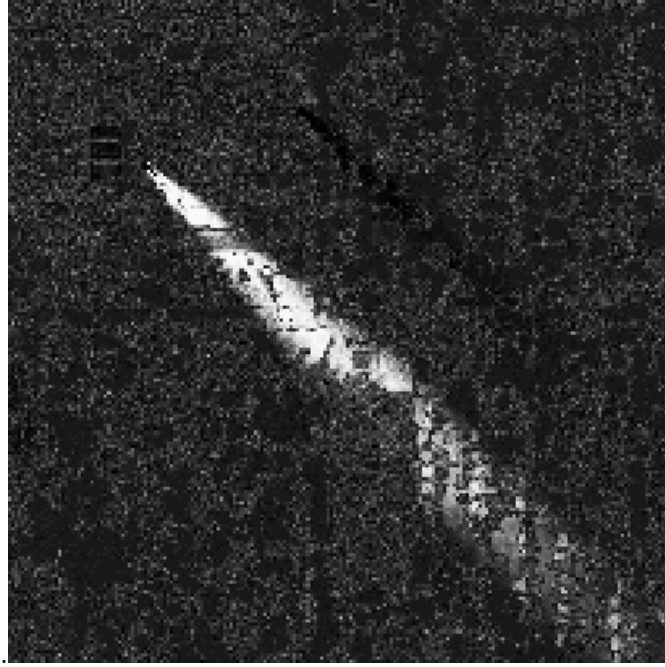


Figure 4.29: Normalized GLRT results for the phosgene band of Case 7, a weak release.

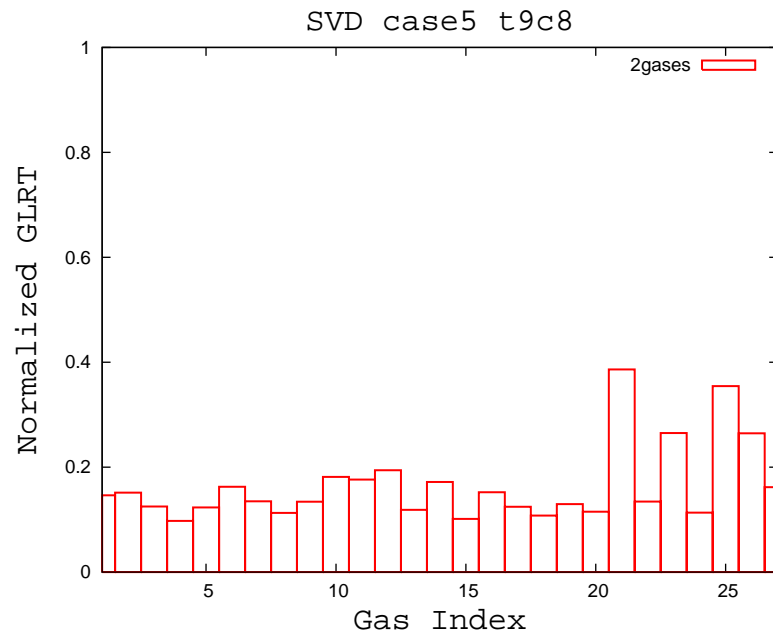


Figure 4.30: Detection profile for the plume region of Case 5, a weak release.



Figure 4.31: Normalized GLRT results for the ammonia band of Case 5, a weak release.

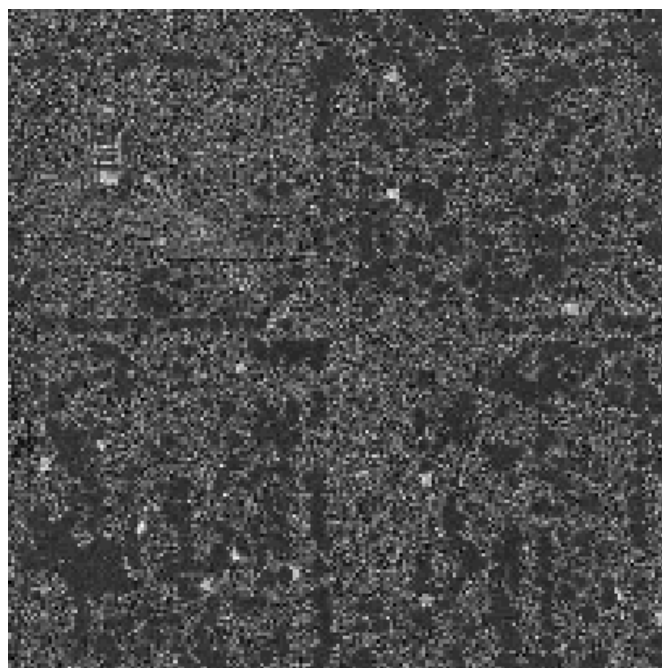


Figure 4.32: Normalized GLRT results for the 1,1,2,2-tetrachloroethane band of Case 5, a weak release.

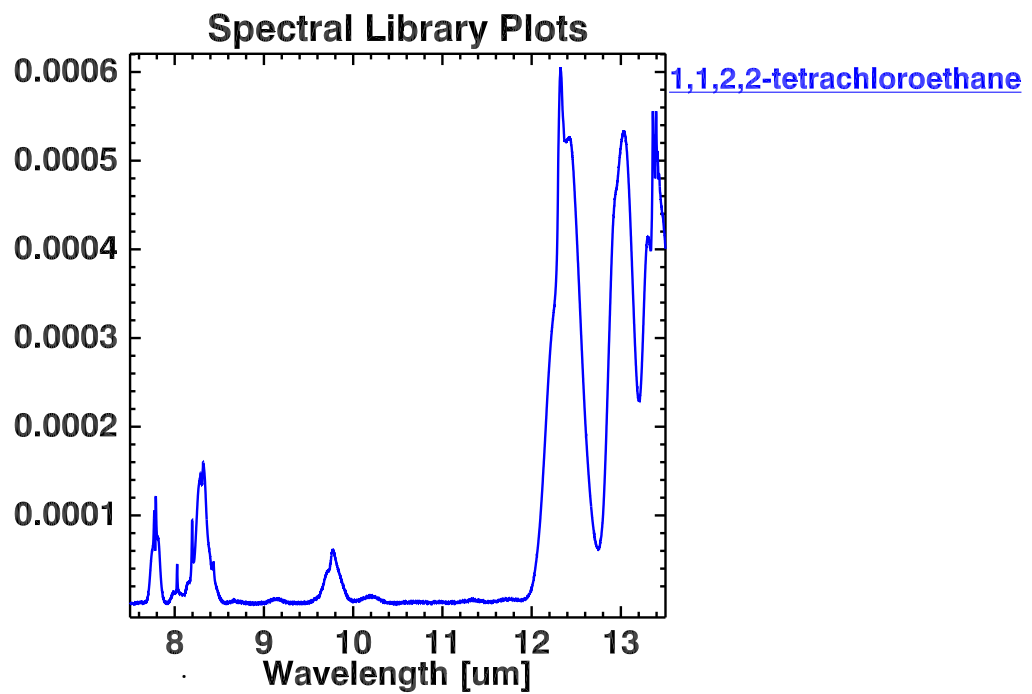


Figure 4.33: Raw absorption spectrum of 1,1,2,2-tetrachloroethane

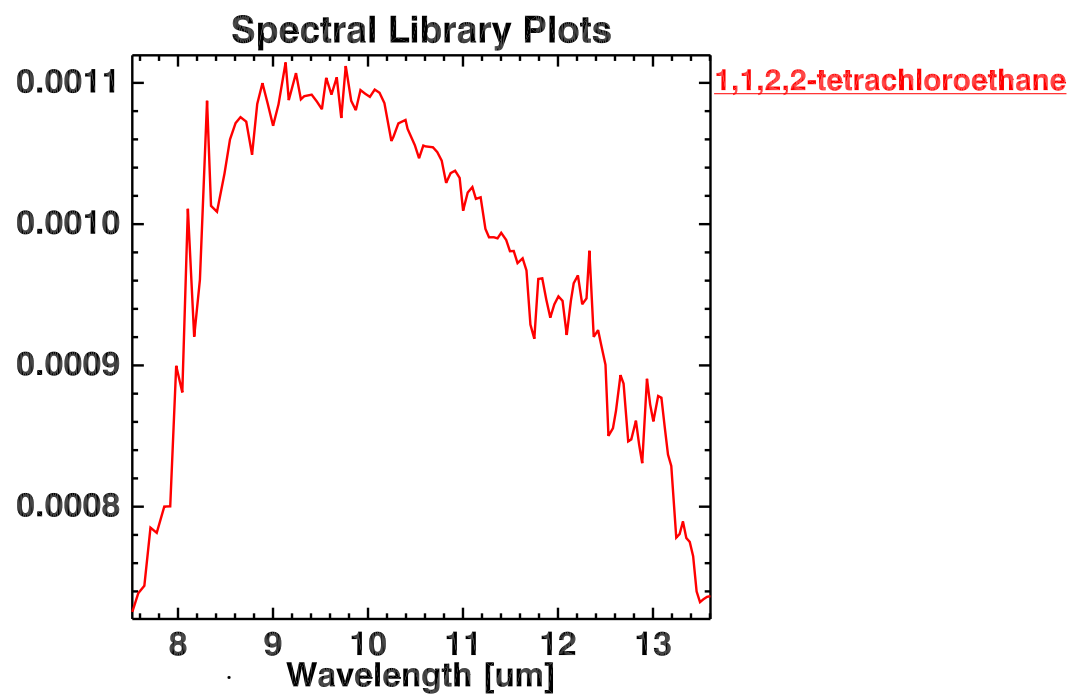


Figure 4.34: Target spectrum for 1,1,2,2-tetrachloroethane at 51°C and 1000 ppm-m

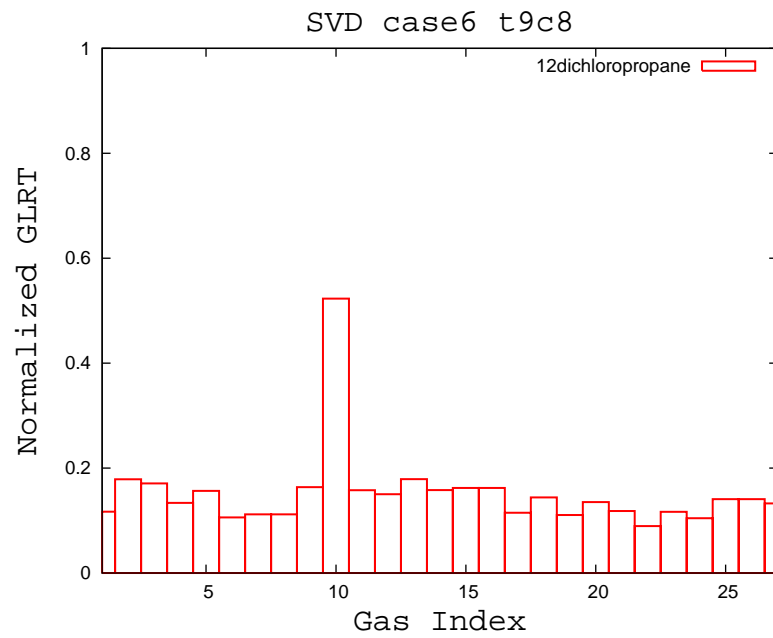


Figure 4.35: Detection profile for the 1,2-dichloropropane plume region of Case 6, a weak release.

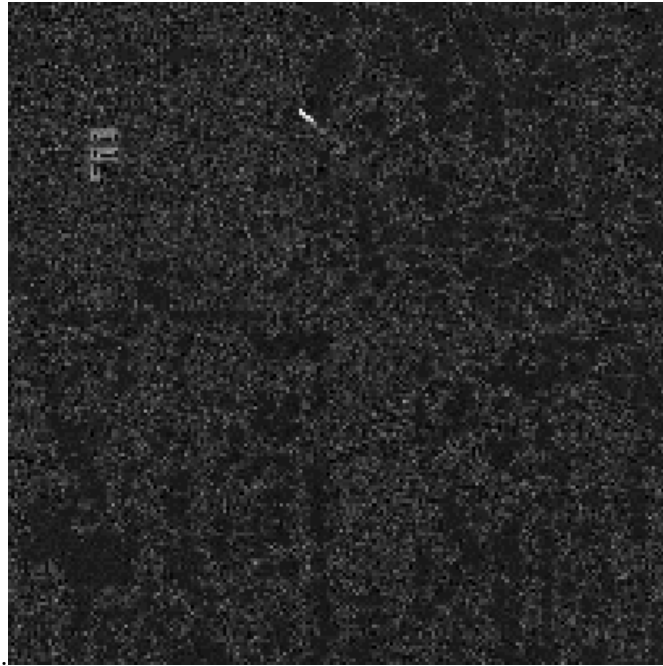


Figure 4.36: Normalized GLRT results for the 1,2-dichloropropane band of Case 6, a weak release.

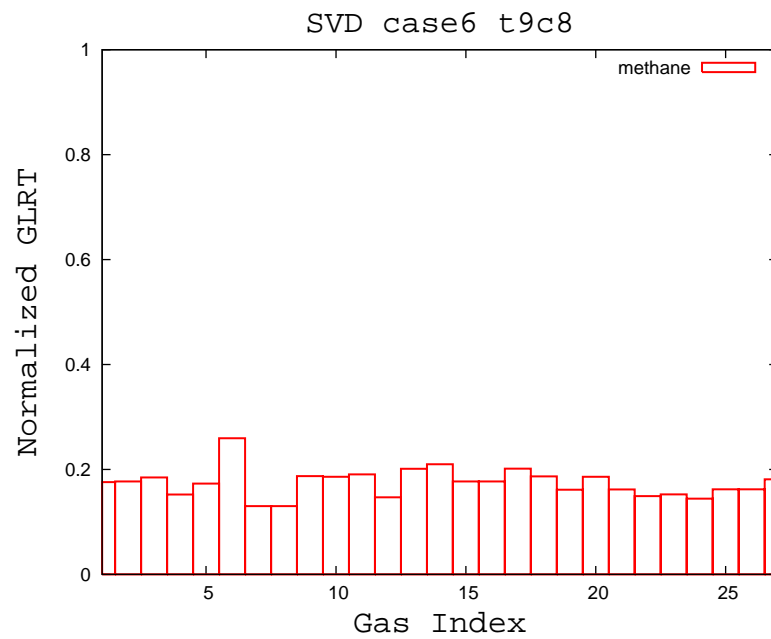


Figure 4.37: Detection profile for the methane plume region of Case 6, a weak release.

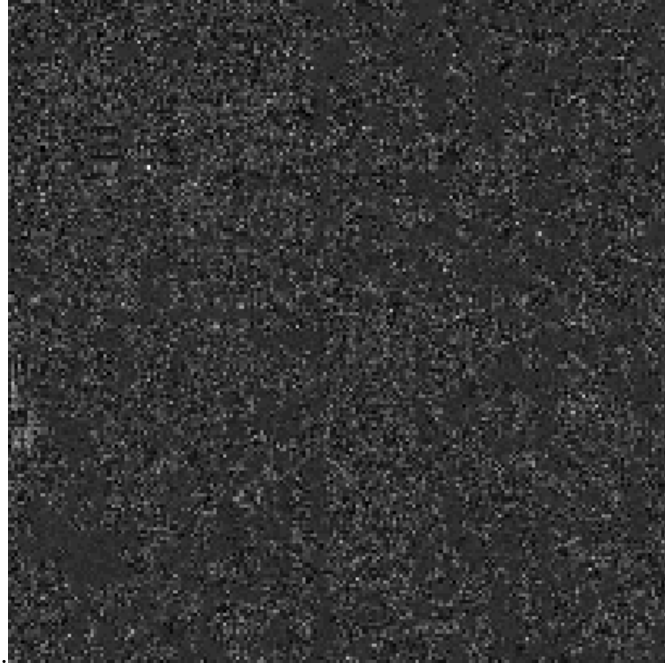


Figure 4.38: Normalized GLRT results for the methane band of Case 6, a weak release.

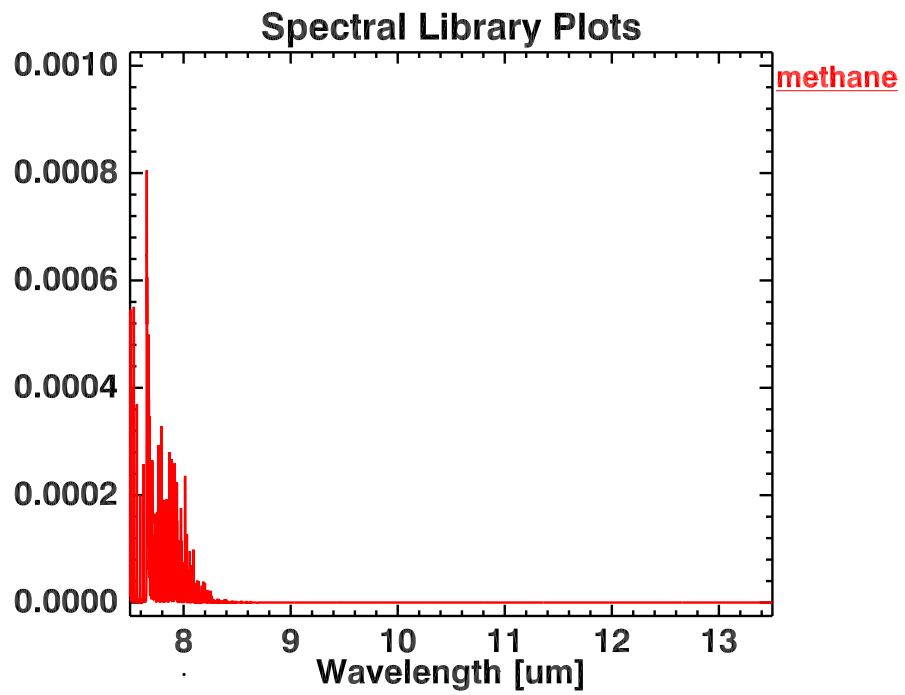


Figure 4.39: Raw absorption spectrum for methane.

Chapter 5

Conclusion

The atmosphere as would be expected is one of the largest problems in the detection and identification process. Many of the spectra once put through the target model lost much of their features, as was seen in the case of methane, 1,1,2,2-tetrachloroethane and trichlorethylene.

Spectral mismatch was also an issue. In every case where ammonia was a plume gas, sulfur hexafluoride returned a lesser detection. This lesser detection is positive since none of the scenes had sulfur hexafluoride, however, it is worth looking at to see why it is showing up when ammonia is detected. They have overlapping features as seen in the laboratory absorption spectra in Figure 5.1 and even more evident in the target spectra shown in Figure 5.2. While it did not produce a higher detection value than ammonia, it still proved to be more prominent than the other gases. One would be inclined to say it was in the plume.

There are some strange detection issues when trees are in the background of the plume. These issues are caused by DIRSIG which has problems modeling the thermodynamic and geometric interaction between the trees and the plume. On the other hand,

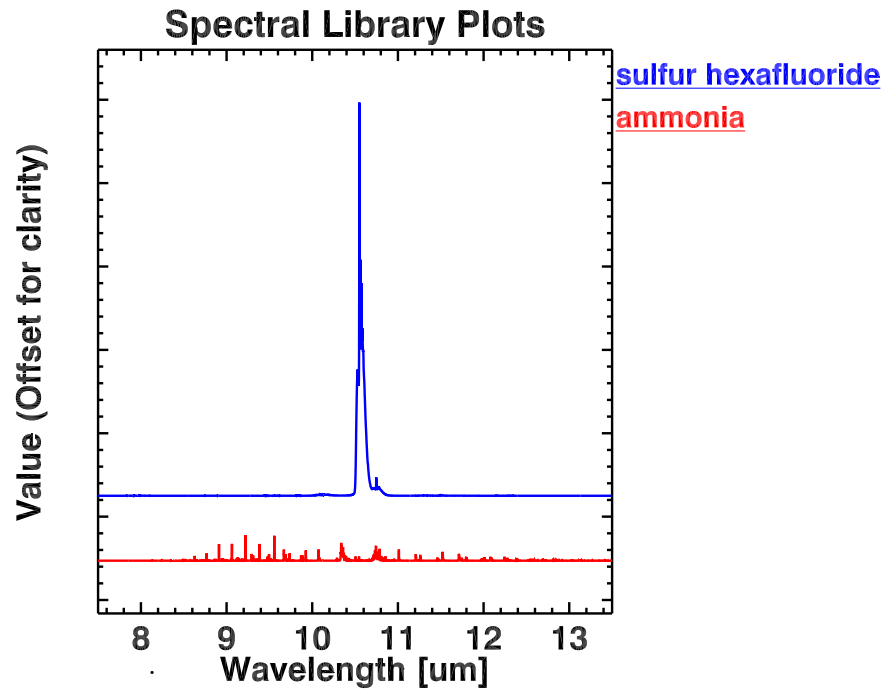


Figure 5.1: Raw absorption spectra for ammonia and sulfur hexafluoride.

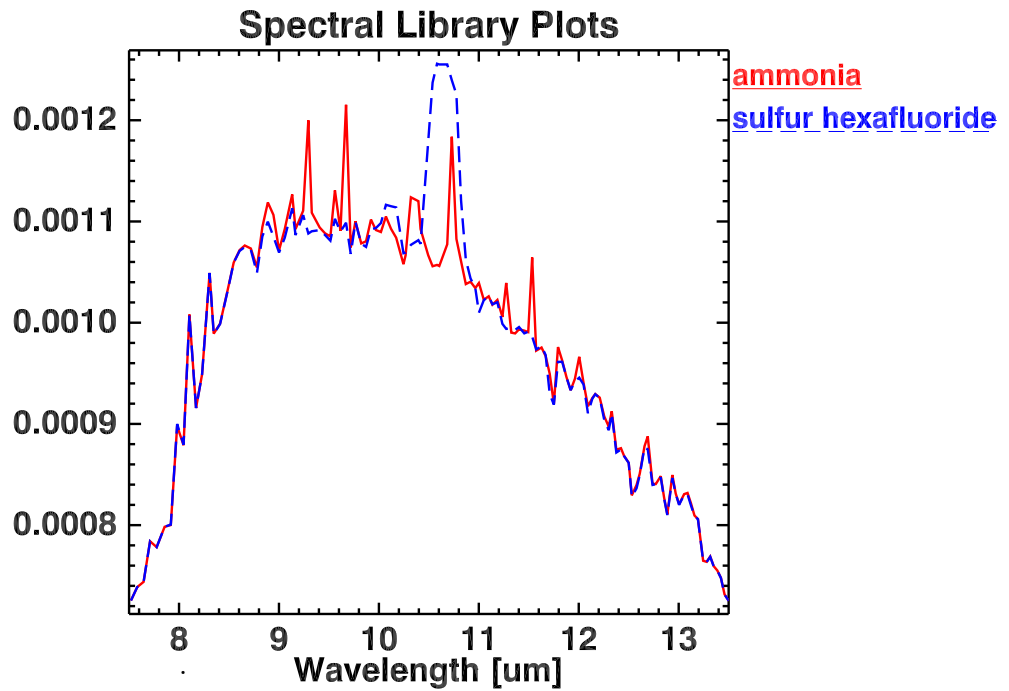


Figure 5.2: Target spectra for ammonia and sulfur hexafluoride.

while the intention of this work was to be able to detect optically thin plumes, the algorithm proved to work on optically thick plumes as well. This is evident in Case 2, specifically in regions close to the stack. All the gas releases tested here were detected, although in some cases weakly. The invariant algorithm has shown to be applicable to the gas detection and identification problem. Both implementations, SVD and MaxD, are equally appropriate target basis vector selection methods. However, it seems as though SVD may be a better basis vector selection method for selecting background basis vectors. This may be because the scene is not as spectrally diverse and is better described by the statistical model, SVD, than the geometric MaxD model.

Chapter 6

Future Work

There is still room for further work on the gas detection and identification problem. Most specifically this work looked at gases individually; an implementation should be done using a target model which uses multiple gases. This is a large undertaking and therefore was not investigated in this initial work. The application of a different sensor model into the target model may change the results and should be further investigated. The multiple slab model discussed previously should be evaluated for generating the target space. The range of concentrations and temperatures should be extended for implementation in both single slab and multiple slab models. Lowering these values may improve detections downwind. Further research should also be done to look at which method of basis vector selection methods is ideal for the background, which proved to be an issue here. Also, other than selecting the top 10 basis vectors for the target and 15 for the background there was no other investigation of the basis vectors. Taking a harder look at exactly what basis vectors are being selected may improve the applicability of the algorithm. Applying the algorithm solely to the spectral region where the target gas features are found may improve the results.

Finally, due to sensitivity and availability issues this study did not test against real

image data. To fully validate these algorithms they should be applied to real data.

Bibliography

- [1] Conover, W. J., 1980, Practical Nonparametric Statistics, John Wiley and Sons, 2nd edition, NY, NY 4.2
- [2] Clausen, S., Bak, J., 1998, Infrared low resolution emission spectroscopy of hot gases. Part of the SPIE Conference on Electro-Optical Technology for Remote Chemical Detection and Identification III, v.3383 2.4
- [3] Hackwell, J., Warren, D., Bongiovi, R., S. J., H., Hayhurst, T., Mabry, D., Sivjee, M., Skinner, J., 1998, Lwir/mwir imaging hyperspectral sensor for airborne and ground-based remote sensing, Part of SPIE Imaging Spectrometry II, Proceedings of SPIE, v. 2819, M. Descour and J. Mooney, eds., pp. 102-107 3.3
- [4] Halitsky, J., 1989, A jet plume model for short stacks, JAPCA Note-Book 39(6), pp. 856-858 3.3
- [5] Healey, G., Slater, D., 1999, Models and Methods for Automated Material Identification in Hyperspectral Imagery Acquired under Unknown Illumination and Atmospheric Conditions, IEEE Transactions on Geoscience and Remote Sensing, v.37, n.6 1.1, 2.3
- [6] Hernandez-Baquero, E., 1999, Inscene Atmospheric Compensation Algorithm: A Graphical User Interface Built with ENVI, Programming for Imaging Science - Class Paper

- [7] Ientilucci, E., Brown, S., 2003, Advances in wide area hyperspectral image simulation, Part of the SPIE Conference on Targets and Backgrounds IX: Characterization and Representation, v. 5065, pp. 110-121 3.3
- [8] Lee, K., 2003, A subpixel scale target detection algorithm for hyperspectral imagery. Ph.D. Dissertation, Rochester Institute of Technology, Center for Imaging Science 1.1, 2.3
- [9] Lisowski, J. J., Cook, C. A., 1996, A SVD Method for Spectral Decomposition and Classification of ARES Data, Proc. SPIE, v.2821, n.15, p.14-29 2.1
- [10] Madsen, R. E., Hansen, L. K., and Winther, O., Singular Value Decomposition and Principal Component Analysis. ISP Technical Report 2004-02-01 (online: <http://www2.imm.dtu.dk/rem/reports/IMM2003-02803.pdf>) 2.1.1
- [11] Neter, J., Kutner, M. H., Nachtsheim, C. J., Wasserman, W., 1996, Applied Linear Statistical Models, Times Mirror Higher Education Group, 4th edition, Chicago, IL 4.2
- [12] Peterson, E., 2004, A Synthetic Landmine Scene Development and Validation in DIRSIG. M.S. Dissertation, Rochester Institute of Technology, Center for Imaging Science 3.3
- [13] Press, W. H., Flannery, B. P., Teukolsky, S. A., 1993, Numerical Recipes in C: The Art of Scientific Computing, Cambridge University Press, 2nd edition 2.1.1, 2.1.1
- [14] Schott, J. R., 1997, Remote Sensing: The Image Chain Approach, Oxford University Press, NY, NY 3.2

- [15] Shlens, J., 2003, A Tutorial on Principal Component Analysis: Derivation, Discussion, and Singular Value Decomposition. Online Note: <http://www.sn1.salk.edu/shlens/pub/notes/pca.pdf> 2.1.1
- [16] Thai, B., Healey, G., 2002, Invariant Subpixel Material Detection in Hyperspectral Imagery. IEEE Transaction on Geoscience and Remote Sensing. v.40, n.3, p.599-608 1.1, 2.3
- [17] Young, S., 2002, Aerospace Corporation, RAND Communication 2.2, 2.2